Geochemistry 84 (2024) 126081

Contents lists available at ScienceDirect

Geochemistry

journal homepage: www.elsevier.com/locate/chemer

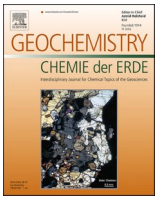

Gold and sulfide-bearing listvenite in the mantle section of the Tays ophiolite in the Arabian Shield, Saudi Arabia

Fahad Alshehri [a], Mokhles K. Azer [b,*], Paul D. Asimow [c], Bassam A. Abuamarah [a]

[a] Abdullah Alrushaid Chair for Earth Science Remote Sensing Research, Geology and Geophysics Department, King Saud University, Riyadh 11451, Saudi Arabia
[b] Geological Sciences Department, National Research Centre, 12622-Dokki, Cairo, Egypt
[c] Division of Geological & Planetary Sciences, California Institute of Technology, Pasadena, CA 91125, USA

ARTICLE INFO

Handling Editor: Federico Lucci

Keywords:
Arabian Shield
Tays ophiolite
Fore-arc
Listvenite
Fuchsite
Sulfides
Gold

ABSTRACT

The mantle section of the Late Neoproterozoic Tays ophiolite in the Arabian Shield consists principally of thoroughly serpentinized peridotite with characteristics typical of depleted mantle protoliths from a fore-arc environment. The serpentinite is altered along shear zones and thrust planes to gold-bearing listvenite bodies of various sizes. These bodies are divided into carbonate listvenite and silica-carbonate listvenite; they may be dyke-like or lenticular in form, and are yellowish-brown, reddish-brown, or greyish in outcrop. Carbonate listvenite expresses schistose deformation fabrics concordant to fabric in the host serpentinite, whereas silica-carbonate listvenite is undeformed at field scale and contains a generation of undeformed minerals at thin-section scale. Silica-carbonate listvenite contains Cr-rich muscovite (fuchsite) and base-metal sulfides and is enriched in Zn, Pb, Cu, Ag, and Au along with SiO_2. The transformation of serpentinite along shear zones to different types of listvenite reflects successive episodes of fluid-mediated metasomatism. Carbonate listvenite develops first, driven by infiltration of CO_2–bearing fluids during serpentinization of the original fore-arc peridotite. Silica-carbonate listvenite marks a later episode associated with infiltration of K-bearing, SiO_2-saturated fluids released during emplacement of the ophiolite. Listvenitization in the Tays serpentinite concentrated gold in sub-economic to economic extents, with concentrations increasing from host serpentinite (2–4 ng/g) to carbonate listvenite (267–937 ng/g) to silica-carbonate listvenite (1717–3324 ng/g).

1. Introduction

Ophiolitic rocks are distinctive components of the Arabian-Nubian Shield (ANS), cropping out along suture zones that run through the Eastern Desert of Egypt and also subdivide the Arabian Shield (the eastern part of the ANS) into its major terranes. The ophiolites represent fragments of oceanic lithosphere that were tectonically emplaced above intra-oceanic magmatic arc assemblages during closure of the Mozambique ocean, causing deformation, alteration, metamorphism, mylonitization and cataclasis (Azer and Stern, 2007; Ali et al., 2010; Ali et al., 2020; Mubarak et al., 2020). One notable style of alteration in the ultramafic sections of ANS ophiolites is carbonatization, an important geological process for several reasons, ranging from the potential for sequestration of anthropogenic carbon to the formation of ore deposits (Boskabadi et al., 2017; Gahlan et al., 2018, 2020a, 2020b; Moussa et al., 2021; Abdel-Karim et al., 2021a, 2021b).

The term “listvenite” was first introduced by Rose (1837) during the study of silicified and carbonated peridotites from the Urals. Although several spellings have been used in English (“listwaenite”, “listwanite”, “listvanite”), we use “listvenite” here as it is closest to the original Russian source. Soviet researchers used the term “listvenite” to describe highly carbonated, sericitized and pyritized mafic and ultramafic rocks (as cited in Boyle, 1979). Hydrothermal alteration of ultramafic rocks leads to replacement of primary silicate minerals or serpentine minerals by an assemblage of carbonates, quartz, sulfides, chromian micas such as Cr-muscovite/fuchsite, and various accessory minerals (e.g., Buisson and Leblanc, 1987; Halls and Zhao, 1995; Plissart et al., 2009). Listvenite is believed to form by intermediate to low-temperature metasomatism and is commonly located on or near major faults or shear zones (Halls and Zhao, 1995; Azer, 2013). Listvenite, as an alteration product of ophiolitic ultramafic rocks, has been noted in several localities among the Neoproterozoic rocks of the Arabian shield, commonly associated with sheared serpentinites along thrust faults and shear zones. With rising interest in gold mineralization in Saudi Arabia, the

* Corresponding author.
E-mail address: mk.abdel-malak@nrc.sci.eg (M.K. Azer).

https://doi.org/10.1016/j.chemer.2024.126081
Received 28 September 2023; Received in revised form 29 December 2023; Accepted 5 January 2024
Available online 17 January 2024

listvenites of the Arabian Shield are receiving attention because of their spatial and temporal association with gold and sulfide mineralization (e.g., Uçurum, 2000; Al Jahdali et al., 2003; Al Jahdali, 2004; Harbi et al., 2006; Akbulut et al., 2006; Al Shanti, 2009; Pirouei et al., 2020; Gahlan et al., 2020a, 2022). However, despite the well-known association between similar Neoproterozoic ophiolitic rocks worldwide and high gold concentrations (Buisson and Leblanc, 1986, 1987; Uçurum, 2000), most listvenite occurrences in the Arabian Shield have not yet been studied or evaluated in detail.

The present work presents the first detailed study of the listvenite in the Late Neoproterozoic Tays ophiolite, at the extreme eastern edge of the Arabian Shield. Our field, petrographic, mineralogical, and

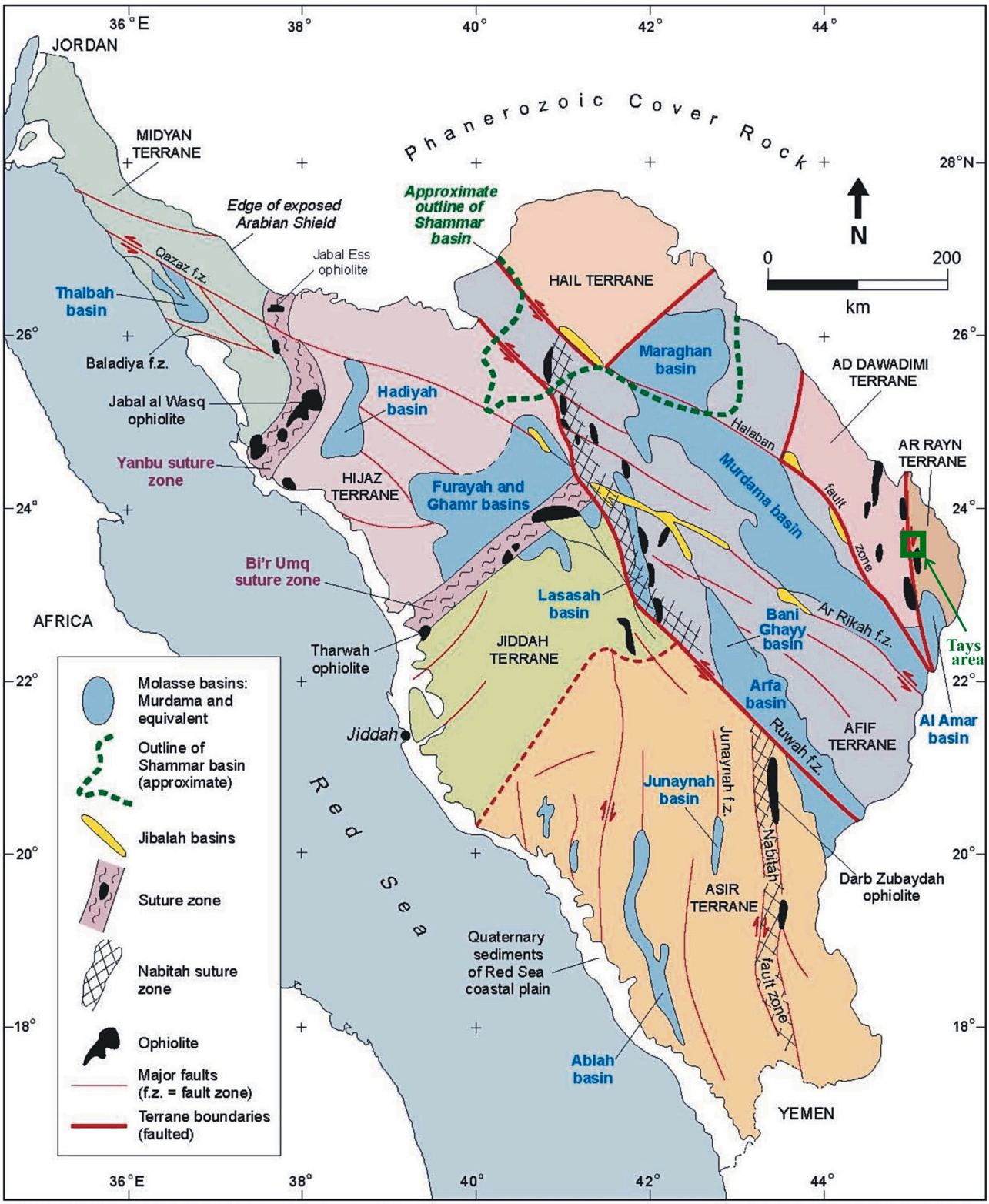

Fig. 1. Simplified geologic map of the Arabian Shield in Saudi Arabia (modified after Nehlig et al., 2002). The location of Jabal Tays ophiolite is indicated by the green box. (For interpretation of the references to color in this figure legend, the reader is referred to the web version of this article.)

geochemical study documents the variations among Tays listvenites. We find evidence for multiple stages of transformation and alteration of peridotite by generations of fluid infiltration, leading to a better understanding of listvenite formation and associated mineralization in the Tays ophiolite and an assessment of the potential of the region as a source for gold.

2. Geologic setting

The Tays area, surrounding a topographic high known as Jabal Tays, is located near the eastern limit of the Arabian shield within the Ad Dawadimi terrane, east of the Halaban suture (Fig. 1). The area comprises mainly Neoproterozoic rocks including ophiolites, the Abt formation and syntectonic granitoids (Fig. 2). Ophiolitic rocks in the Tays area are in tectonic contact with the Abt formation and include serpentinites and metagabbro. Most of the serpentinite masses occur as massive thrust sheets with numerous internal shear planes. The ophiolite appears to be part of a structurally detached allochthon, far traveled from its root zone (Johnson et al., 2004).

The Abt formation is a distinctive Ediacaran siliciclastic sedimentary unit in the Ad Dawadimi terrane. The formation extends about 225 km north-south and ~100 km east-west, sandwiched between the Afif and Ar Rayn terranes (Johnson and Stewart, 1995). In the study area, the Abt formation is represented by low-relief exposures of sandstone, siltstone, conglomerate, and limestone. Bed thicknesses range from a few centimeters to a few meters and sedimentary structures include cross bedding and grading. The youngest ages of detrital zircons (621 ± 3 Ma, Kennedy et al., 2011; 618 ± 16 Ma, Cox et al., 2012) in the Abt formation indicate that it was deposited at or soon after ~620 Ma.

In the ultramafic section of the ophiolite, listvenite bodies of different shapes (dyke-like or lenticular) and sizes (up to several meters long) are developed along the shear zones. They are hard, massive rocks despite local shearing and fracturing. They vary in their appearance in the field, ranging from yellowish-brown and reddish-brown to greyish depending on the relative abundances of quartz and carbonates and the extent of iron-oxide staining. A few outcrops have a spongy texture due to supergene oxidative weathering.

We distinguish two main varieties of listvenite: carbonate listvenite and silica-carbonate listvenite (supplementary Fig. 1S). In general, carbonate listvenite is deformed, sheared, brecciated and fractured similarly to the host serpentinite, while silica-carbonate listvenite is undeformed. The presence of deformation fabrics in the carbonate listvenite suggests its formation predates deformation, while the absence of deformation fabrics in silica-carbonate listvenite suggests its formation postdates serpentinization and carbonate listvenite. Evidence of shearing is pronounced in carbonate listvenite, where quartz crystals show strong preferred orientation. Fractures are filled by *en echelon* smoky quartz veins, carbonate veinlets and fine quartz ribbons. The structural elements in the sheared carbonate listvenite are generally conformable to the main plano-linear fabric of the host serpentinite. We infer from this that the deformation of serpentinite and carbonate listvenite was coeval, and that the schistosity developed after alteration to

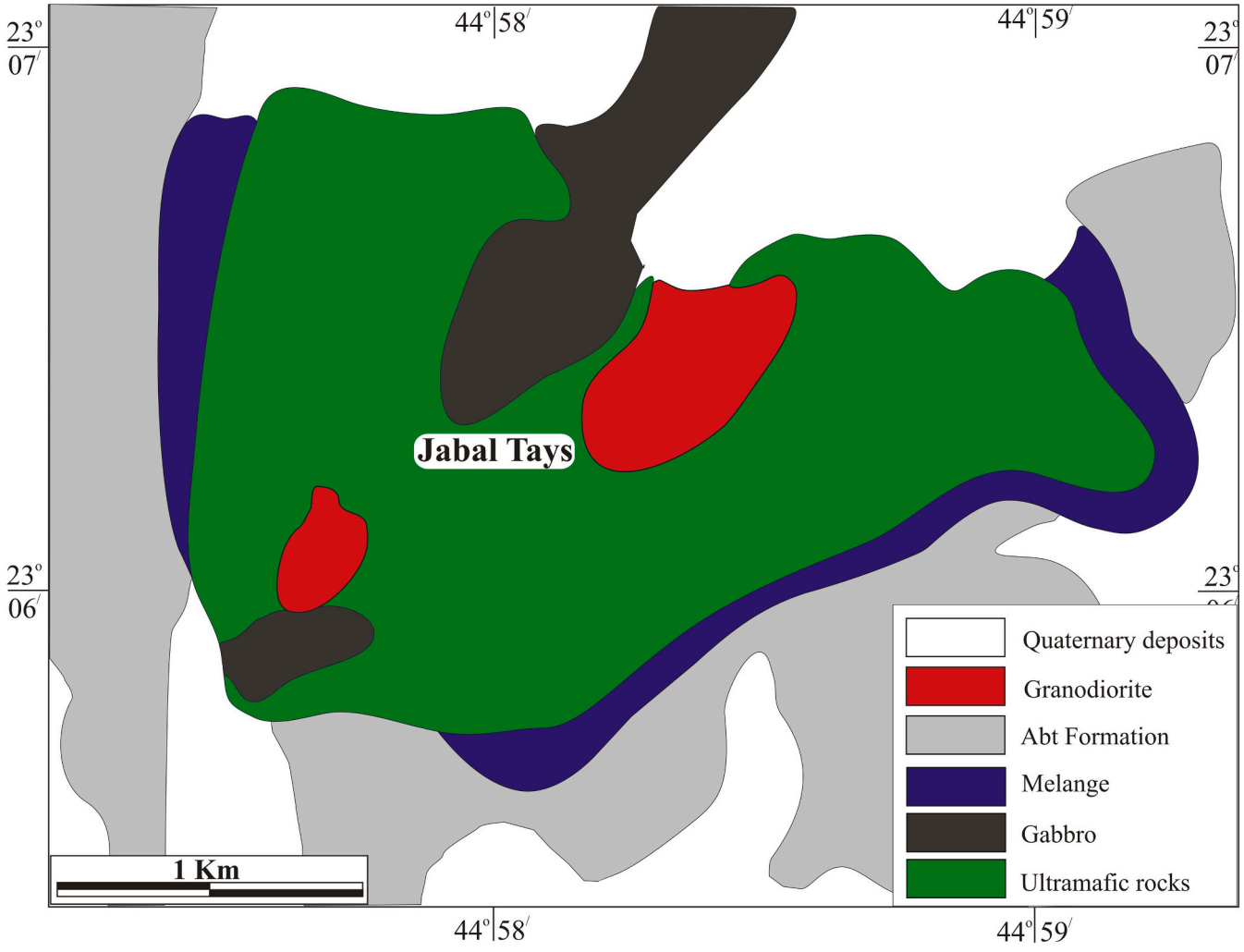

Fig. 2. Geologic map of Jabal Tays area.

carbonate listvenite. By contrast, field-scale schistosity and deformation fabrics are absent in silica–carbonate listvenite. In a few outcrops, the listvenites are capped with a few meters of resistant, deep red or brown silica-rich listvenite.

3. Petrography

Petrographic descriptions of serpentinite and listvenite, with mineral identifications supplemented by electron microscopy and electron microprobe analyses (see Section 4.2) are given below.

3.1. Serpentinite

Serpentinized peridotite (serpentinite) is greenish-black and consists mainly of serpentine minerals with minor carbonates and rare fresh relics of olivine, pyroxenes and Cr-spinel. Serpentine (80–95 %) is mainly fine fibers of antigorite, forming an interlocking texture. Fine veinlets of chrysotile traverse the thin sections. There are also a few veins of lizardite (Fig. 3a). Fresh olivine relics are recorded in a few samples, dissected by networks of fine serpentine veinlets (Fig. 3b). Relics of pyroxene have strings of fine magnetite along cleavage planes and are surrounded by serpentine (Fig. 3c). The presence of mesh texture after olivine (Fig. 3d) and of variable amounts of bastite texture after orthopyroxene (Fig. 3e) indicates dunite and harzburgite protoliths.

Carbonates are mainly magnesite, which is found both in sparse spots mixed with microcrystalline talc and as fine veinlets traversing whole thin sections. Amphiboles are recorded in a few samples, including actinolite, tremolite, and anthophyllite (Fig. 3f). They occur as acicular crystals and as colonies of columnar fibers.

Opaque minerals include Cr-spinel, magnetite and sulfides. Cr-spinel occurs as subhedral to anhedral crystals with fresh, blood red cores and rims of ferritchromite and Cr-magnetite. Spinel is sometimes surrounded by subhedral flakes of Cr-chlorite. Magnetite is found as disseminated fine crystals and along the cleavage planes of pyroxene. The sulfide is pyrite, found as sparse, tiny rounded and subrounded disseminated crystals.

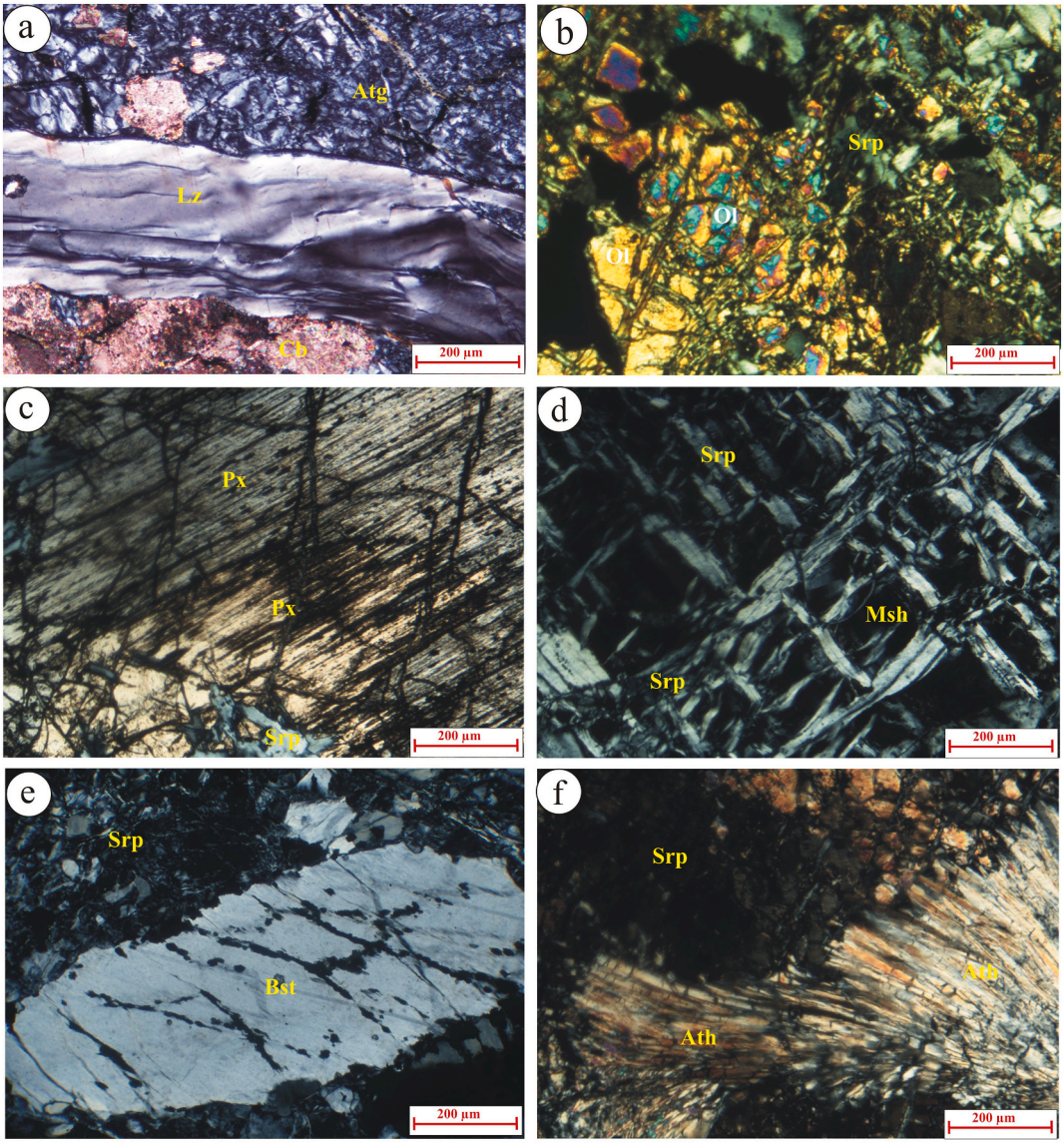

Fig. 3. Petrographic features in Tays serpentinized peridotite (all figures in cross-polarized transmitted light): (a) Bundle-like vein of lizardite between antigorite and carbonate, (b) fresh relics of primary olivine, (c) relics of pyroxene with fine striations of magnetite on cleavage planes, (d) mesh texture marking serpentine replacing olivine, (e) bastite texture marking serpentine replacing orthopyroxene, and (f) acicular crystals and columnar fibers of anthophyllite. Mineral abbreviations are: Atg = antigorite; Lz = lizardite; Ol = olivine; Px = pyroxene; Srp = serpentine; Msh = mesh; Bst = bastite and Ath = anthophyllite.

3.2. Listvenites

3.2.1. Silica-carbonate listvenite

Silica-carbonate listvenite is the most abundant variety. It consists mainly of quartz and carbonates with minor amounts of serpentine, chlorite, Cr-rich muscovite (fuchsite), and opaques. In the investigated samples, the proportion of quartz (55–65 %) generally exceeds that of carbonate minerals (35–45 %), although in a few samples the proportions of quartz and carbonates are almost equal. Both carbonate minerals and quartz occur in more than one generation. First-generation quartz forms microcrystalline fine aggregates and fine- to coarse-grained subhedral crystals. Strain effects in first-generation quartz are

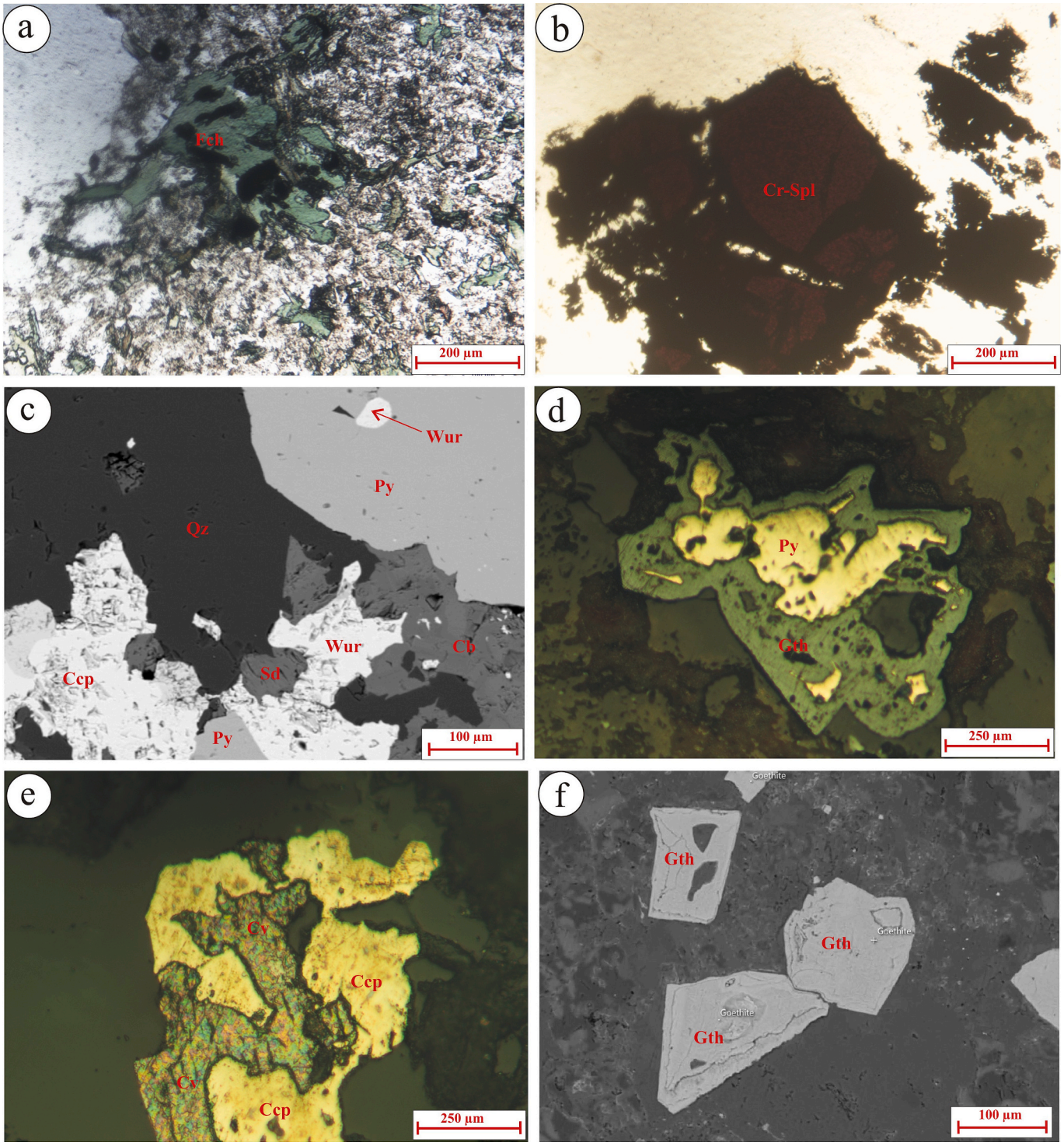

Fig. 4. Petrographic features in silica-carbonate listvenite (a and b in plane-polarized transmitted light; d and e reflected light; c and f in electron backscatter): (a) fuchsite with dark green color, (b) fresh cores of Cr-spinel altered along margins and cracks to ferritchromite, (c) different phases of sulfide minerals associated with carbonate and quartz, (d) pyrite partly replaced by goethite, (e) chalcopyrite partly altered to covellite, and (f) goethite exhibiting well-developed colloform texture. Mineral abbreviations are: Fch = fuchsite; Cr-Spl = chrome spinel; Qz = quartz; Wur = wurtzite; Py = pyrite; Ccp = chalcopyrite; Cv = covellite; Gth = goethite; Sd = siderite; and Cb = carbonate. (For interpretation of the references to color in this figure legend, the reader is referred to the web version of this article.)

noticeable, including wavy, undulatory extinction and brecciation. Second-generation quartz is found as unstrained, medium- to coarse-grained crystals forming mosaic textures or filling fractures between the carbonates. Carbonates (see Section 4.2) include several varieties: calcite, dolomite, magnesite, siderite, and occasional ankerite. The first generation of carbonates occurs as both very fine and coarse aggregates that are darkly stained brownish due to argilliceous alteration by Fe-oxides. First-generation carbonates exhibit distinct polysynthetic twinning as well as kink banding, fragmentation, and recrystallization into fine-grained aggregates along micro fractures. Second-generation carbonate is found as medium to coarse-grained crystals that are accumulated in clusters or as veinlets cross-cutting microcrystalline quartz.

Relics of serpentine are sometimes intercalated with fine aggregates of carbonate. Chlorite occurs as fine fibers forming short veins. Fuchsite, with its characteristic dark green color in plane-polarized light (Fig. 4a), is observed in some (but not all) samples of silica-carbonate listvenite. It occurs either as flakes or as fine disseminated aggregates that are sometimes intergrown with chlorite.

The total abundance of opaque minerals in silica-carbonate listvenite is noticeably variable (1–5 %). These include Cr-spinel, sulfides, goethite, and gold. Cr-spinel is found as highly altered and brecciated crystals with fresh, blood red cores and fractures filled with carbonates (Fig. 4b). Sometimes, Cr-spinel is characterized by spongy or porous textures, particularly at the margins. Sulfides include pyrite, chalcopyrite, and wurtzite (Fig. 4c). Rare galena is recorded in a few samples. Pyrite occurs as bright yellow specks and fine crystals as well as fine euhedral cubes. It is partly replaced by goethite (Fig. 4d). Anhedral to subhedral chalcopyrite is less abundant than pyrite and is partly or completely altered to covellite (Fig. 4e). Goethite exhibits well-developed colloform texture (Fig. 4f). Fine specks of gold are found associated with pyrite crystals and are dispersed in both quartz and carbonate.

3.2.2. *Carbonate listvenite*

Carbonate listvenite is composed mainly of carbonate minerals (60–85 %) and microcrystalline silica with sparse opaque minerals. Carbonate minerals are subhedral, fine to coarse crystals and also occur as crosscutting veinlets (Fig. 5a, b). Some carbonate crystals show colloform silica along their cracks. Black pigmentation in some carbonate crystals is attributed to the presence of manganese oxide, while red pigmentation is ascribed to iron oxides. Quartz (15–40 %) is mostly microcrystalline, with fine subhedral crystals and minor veinlets traversing the carbonate minerals. There is only one generation of quartz and carbonate minerals apparent in this listvenite variety, and all crystals show clear evidence of shear deformation.

Opaque minerals include Fe-Ti oxides, Cr-spinel and sulfides. Cr-spinel is partly altered to ferritchromite. Sometimes, Cr-spinel occurs as island-like relics within ferritchromite (Fig. 5c), forming a distinct rim-replacement texture. Sulfide minerals include pyrite, pyrrhotite and chalcopyrite. Pyrite occurs as homogenous subhedral to anhedral crystals (Fig. 5d). Pyrite may be intergrown with chalcopyrite. In this variety of listvenite, gold is rare and occurs as very fine disseminated specks in carbonate minerals.

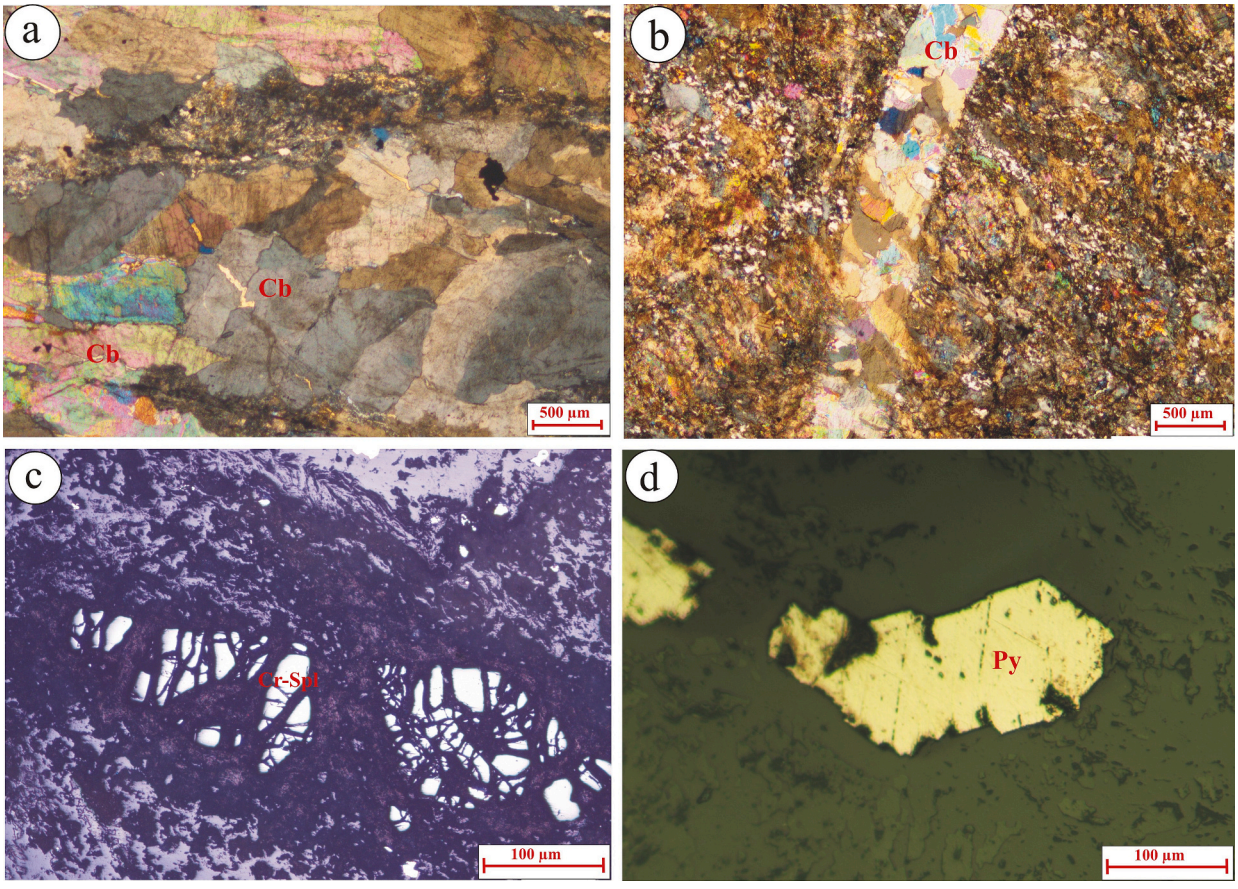

Fig. 5. Petrographic features in carbonate listvenite (a and b in plane-polarized transmitted light; c and d reflected light): (a) coarse anhedral magnesite crystals, (b) veinlet of secondary carbonates crosscutting fine carbonates, (c) island-like relics of fresh Cr-spinel within ferritchromite, and (d) homogenous subhedral crystal of pyrite. Mineral abbreviations are: Cr-Spl = chrome spinel; Py = pyrite and Cb = carbonate.

4. Analytical techniques

4.1. Whole-rock analysis

Forty-three representative samples (13 carbonate listvenite, 20 silica-carbonate listvenite and 10 serpentinite) were analyzed for major, trace and rare earth elements at Activation Laboratories Ltd. (Actlabs, Canada). Major oxides were measured by lithium metaborate/tetraborate fusion ICP-AES. Trace and rare earth elements were measured by ICP-MS following lithium borate fusion and acid digestion. Loss on ignition (LOI) was determined by weight difference after heating for 1 h at 1000 °C. Precision and accuracy were controlled by analysis of international reference materials (e.g. GSP2) and replicate analyses and are 1 % for major elements and 2 % to 5 % for trace elements. Further analytical details are given by the vendor (https://actlabs.com/geochemistry/lithogeochemistry-and-whole-rock-analysis/lithogeochemistry/).

4.2. Mineral chemistry

Mineral chemical analyses were obtained from polished, carbon-coated thin-sections using a five-spectrometer JEOL JXA-8200 electron microprobe (EPMA) housed at the Division of Geological and Planetary Sciences (GPS), California Institute of Technology, USA. Operating conditions were 15 kV accelerating voltage, 25 nA beam current, a focused beam (1 μm) and 20 s on-peak counting times. A set of synthetic and natural mineral standards were used for calibration, including anorthite, fayalite, synthetic forsterite, Mn-olivine, pyrite, Cr_2O_3, and TiO_2 as well as Durango apatite, Asbestos microcline, Amelia albite and Pacoima zircon. Quartz, MgO and Al_2O_3 provided additional control points for the mean atomic number (MAN) background subtraction method. The obtained data were corrected by a CITZAF matrix correction routine program. Analyses are presented as oxide weight percents for all minerals. Silicate analyses are also given as atoms per 24 oxygens, whereas sulfides are given as atomic percent and carbonates are given as cations per calculated carbonate group.

Backscattered electron images and energy dispersive X-ray spectra (EDS) were obtained with a Zeiss 1550VP field-emission scanning electron microscope (SEM) in the Division of Geological and Planetary Sciences at Caltech. To detect heavy elements, a 25 kV primary beam was chosen and spectra were collected in the 0–20 kV range. Dead time was maintained below 60 % and spectra were integrated for 60 s of live time. The EDS detector is a Si-drift type Oxford Max, and data were processed with Oxford's AZTec software, using factory standards for quantification.

4.3. Raman spectroscopy

Selected mineral identifications were further verified by Raman spectroscopy. A Renishaw InVia micro-Raman instrument at Caltech with a 514 nm laser was used to collect spectra from Raman shifts of 100 to 4000 cm^{-1}. An 1800 lines/mm^{-1} diffraction grating was used; scans over the wavelength range were 10 s each and three scans were averaged for each point. Laser power was kept at 10 % in order to reduce sample heating and damage while providing adequate count rates. Cosmic ray-induced spikes and backgrounds were removed and these processed spectra were compared to the RRUFF.info library for mineral identification.

5. Mineral chemistry

Mineral assemblages of the listvenites identified under the microscope were confirmed by SEM, Raman analysis and EPMA.

5.1. Scanning electron microscopy

Minerals identified by scanning electron microscopy include sulfides (pyrite, galena, wurtzite, femolite, and molybdenite), oxides (rutile, tenorite and baddeleyite), hydroxide (goethite), carbonates (magnesite, calcite and dolomite), sulfate (barite), and phosphides (nickelphosphide and melliniite). Selected backscatter images and EDS spectra from a silica-carbonate listvenite sample are reported in supplementary Figs. 2S–5S.

5.2. Raman spectroscopy

Micro-Raman spectroscopy was applied to selected minerals (chalcopyrite, siderite and wurtzite) in silica-carbonate listvenite in order to confirm the mineral species inferred from petrography and mineral chemistry. The spectra and corresponding reference spectra of X-ray characterized specimens from the RRUFF library are shown in supplementary Fig. 6S.

5.3. Electron microprobe

Electron microprobe analyses were performed to determine the chemical composition of essential minerals in the Tays silica-carbonate listvenite. The analyzed minerals, reported in the supplementary tables, include carbonates (ST1), sulfides (ST2), "goethite" (ST3), and paragonite (ST4).

The oxide composition and cation fractions are reported for carbonate minerals, including magnesite, calcite, dolomite, siderite and ankerite (Fig. 6a, b). Analytical totals were constructed by assuming one mole of CO_2 per mole of divalent cations; this resulted in acceptable totals (97–102.5 wt%) for all species except siderite, which is systematically low (92.6–96.96 wt%). The reason for the low totals in siderite is not clear; there are no unanalyzed elements present (confirmed by EDS), they are not hydrous (confirmed by Raman), and the analyzed phase is definitely siderite and not some other species (confirmed by Raman). Ferric carbonate is not stable, so the assumption of $FeCO_3$ stoichiometry should be valid. The total becomes systematically lower as the Fe atoms approach 1 apfu. There may be a subsurface charging process associated with the conductivity of Fe-rich siderite that causes Fe counts to differ from those in the insulating fayalite standard. In any case, we consider that the cation ratios (e.g., Fe/Mg ratio) in the siderite analyses are accurate. Magnesite is impure, with 0.66 to 0.81 apfu, and solution towards both Fe (up to 0.18 apfu) and Ca (up to 0.24 apfu). Calcite may be relatively pure (0.94 to 0.96 apfu) or may show extensive solution towards Mg (up to 0.21 apfu) or Fe (up to 0.16 apfu). Dolomite compositions are variable, with Mg/Ca ratios between 1.0 and 0.64 and Fe substitution from 0.04 to 0.13 apfu. Siderite is the chief iron carbonate mineral; it ranges from 0.95 down to 0.55 apfu Fe and the chief substituent is Mg, up to 0.36 apfu. Zn is essentially absent from the siderite ($\leq$0.007 apfu). A single ankerite point was found, with 0.45 apfu Fe and 0.41 apfu Ca.

Sulfides (pyrite, chalcopyrite and wurtzite) are presented as elemental weight percent and atomic percent (Fig. 6c). Pyrite is nearly pure; although As, Cu, Zn, Pb, Mn, Cr and Ni are occasionally found above detection limits, their concentrations never exceed 1 at.%. Chalcopyrite is close to nominal $FeCuS_2$ composition, although Cu/Fe ratios vary from 0.91 to 0.96; other elements are strictly <0.4 at.% (detected elements include Ni, Cr, Ti, Mn, As, Zn and Pb). Wurtzite, (Zn, Fe)S, is distinguished from sphalerite by the presence of 1.9 to 7.8 at.% Fe; other detected elements besides the major Zn include minor amounts ($\leq$0.9 at. %) of Mn, Cr, Ni, Cu, As and Pb.

Goethite, a common alteration product of iron-bearing minerals such as pyrite and magnetite (Deer et al., 1992), typically occurs as extremely fine-grained aggregates with other alteration phases. At the scale of the electron probe beam, it shows variable amounts of SiO_2 (1.70–5.15 wt %) alongside the major FeO_t (61.37–77.51 wt%) and low totals

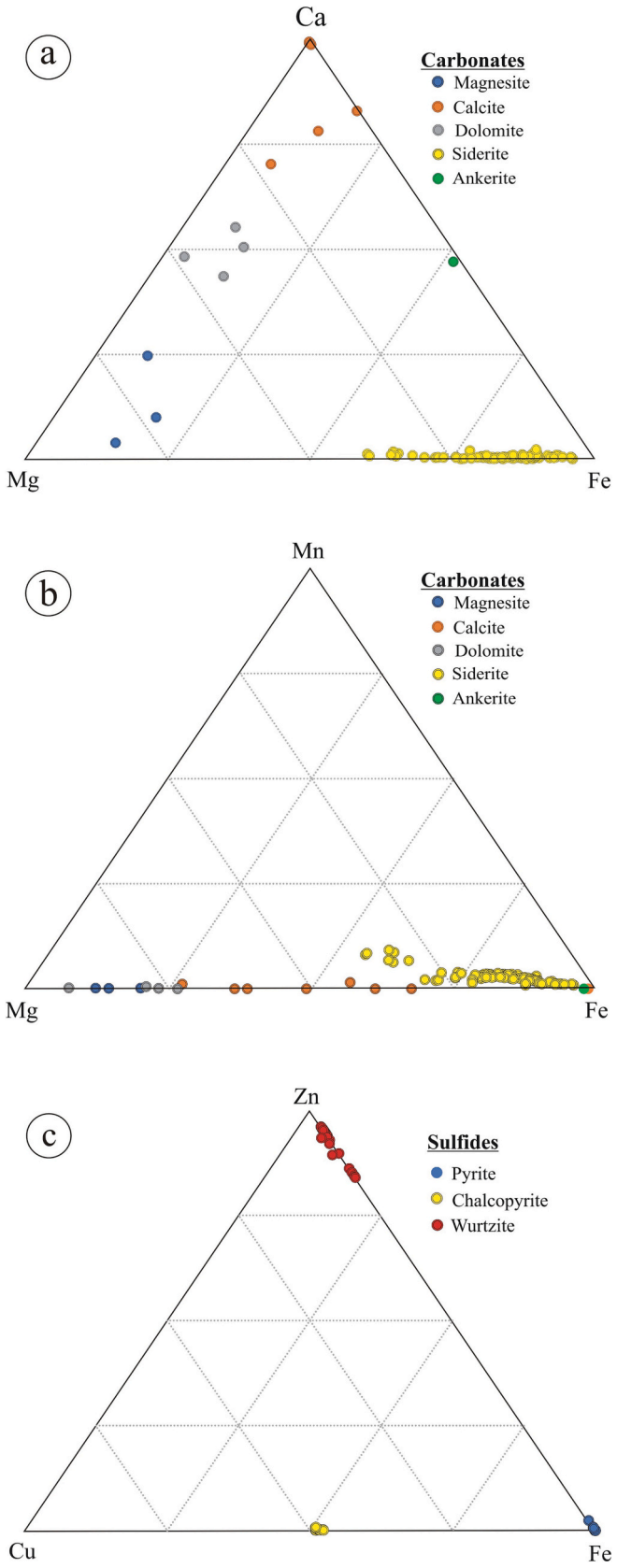

Fig. 6. Composition of carbonate and sulfide minerals in silica-carbonate listvenite samples. (a) Carbonates projected into the ternary Ca-Mg-Fe. (b) Carbonates projected into the ternary Mn-Mg-Fe. (c) Sulfides projected into the ternary Zn-Cu-Fe.

(65.2–85.7 wt%) reflecting its variably hydrous character. A few electron probe spots were recognized as other alteration phases such as paragonite.

6. Geochemistry

6.1. Serpentinized ultramafics

Eleven representative samples of serpentinized peridotite (4 dunite and 7 harzburgite), were analyzed for major oxides, trace elements and REE (Supplementary Table ST6). The serpentinite samples have high loss on ignition (12.2–13.6 wt%), consistent with nearly complete serpentinization. Their normative compositions are dominated by olivine and orthopyroxene, confirming the petrographic inference of their protoliths. Although serpentinization is an open-system process that may be associated with loss of CaO and hence decrease of normative clinopyroxene, it is very unlikely in the context of ANS ophiolites to find any lherzolite protolith samples or abundant residual clinopyroxene, independent of the degree of serpentinization (e.g., Abdel-Karim et al., 2021a). In the absence of any petrographic evidence of relict clinopyroxene or serpentine texture suggesting alteration after clinopyroxene, we conclude that the protoliths of all the analyzed serpentinite samples are either dunite or harzburgite.

The serpentinite samples have moderate $Fe_2O_3^T$ contents (6.6–7.6 wt %) that are not correlated with lithology. Serpentinite samples with dunite protoliths have lower silica content (35.9–37.1 wt%) and higher MgO (42.1–42.55 wt%) than those from harzburgite protoliths (38.6–39.5 wt% SiO_2 and 37.9–40.1 wt% MgO). No notable variation in other major oxides is found; all the samples are depleted in TiO_2 ($\leq$0.03 wt%), Al_2O_3 (0.42–0.95 wt%), MnO (0.05–0.11 wt%), Na_2O ($\leq$0.02 wt %), K_2O ($\leq$0.02 wt%), CaO (0.44–1.11 wt%) and P_2O_5 ($\leq$0.02 wt%) and these oxides do not correlate with SiO_2 or MgO. The low concentrations of CaO and Al_2O_3 are consistent with the scarcity of clinopyroxene and complete absence of plagioclase in the protolith.

The whole-rock Mg# [100 Mg/(Mg + Fe) on a molar basis] of Tays serpentinite is generally high; it is slightly higher in serpentinized dunite (~0.92) than in serpentinized harzburgite (~0.91). These values are similar to those of modern oceanic peridotites (Mg# >0.89, Bonatti and Michael, 1989) and to other serpentinized ophiolitic ultramafic rocks in the ANS (e.g., Azer et al., 2013; Khalil et al., 2014; Gahlan et al., 2015; Obeid et al., 2016; Gahlan et al., 2020b, 2020c; Gahlan et al., 2021; Moussa et al., 2022).

On the MgO/SiO_2 vs. Al_2O_3/SiO_2 diagram (Jagoutz et al., 1979; Hart and Zindler, 1986), all the serpentinite samples plot at low Al_2O_3/SiO_2 (Fig. 7a), indicating derivation from a depleted mantle source affected by high degrees of partial melt extraction. Moreover, on the binary Al_2O_3 vs. CaO diagram (Ishii et al., 1992), the serpentinite samples show low Al_2O_3 and CaO, resembling modern oceanic fore-arc peridotites (Fig. 7b).

The studied serpentinites show wide variations in trace element contents (ST6). They are highly depleted in most trace elements (Ba, Be, Ga, Hf, Nb, Rb, Sn, Sr, Th, Ta, U, W, Zr, Mo, Y, Cd, Sb, Bi, Ag, Au, Hg, and Se) compared to the primitive mantle values (McDonough and Sun, 1995). On the other hand, they are enriched in the compatible elements Cr (1505–2597 μg/g), Ni (2146–2443 μg/g), and Co (97–127 μg/g). They are slightly enriched in other compatible elements (Sc, Cu, Zn, and V). The primitive mantle (PM)-normalized trace elements patterns of the serpentinite samples (Fig. 8A) are nearly parallel and closely related, although the dunite protolith samples have generally lower concentrations of most plotted elements. The samples are notably less depleted in highly incompatible elements than in moderately incompatible elements. They exhibit positive anomalies of some fluid-mobile elements including Cs, U, Pb, and Sr. There are also other positive anomalies, e.g., Th, Nb, and Tm.

The enrichment in some elements (Sr, U and Pb) can be related to addition from hydrothermal solutions during fluid-rock interaction

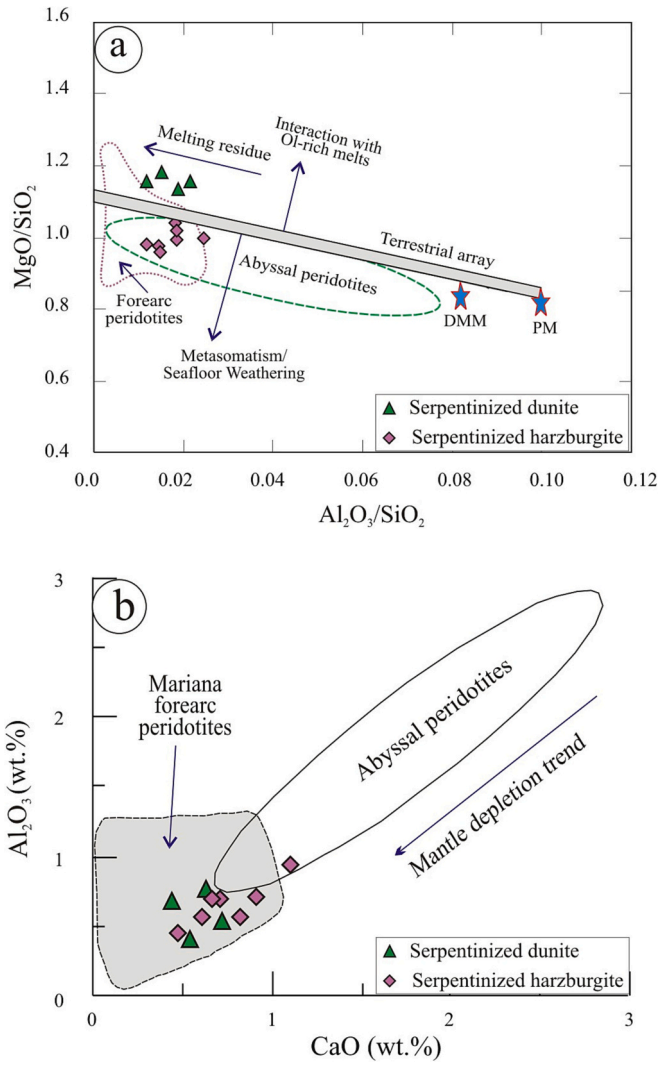

Fig. 7. Whole-rock compositions of serpentinized peridotite. (a) MgO/SiO_2 vs. Al_2O_3/SiO_2; abyssal peridotites field after Niu (2004), field of fore-arc peridotites after Pearce et al. (2000) and Parkinson and Pearce (1998), depleted mantle and primitive mantle values from Salters and Stracke (2004) and McDonough and Sun (1995), terrestrial array according to Jagoutz et al. (1979) and Hart and Zindler (1986); DMM and PM as well as the trends of "interaction with Ol-rich melts" and "Metasomatism" are adopted from Sepidbar et al. (2020). (b) Al_2O_3 vs. CaO discrimination diagram for serpentinized peridotite (Ishii et al., 1992).

(Deschamps et al., 2013; Moussa et al., 2022). Each of these elements can be sequestered and concentrated from migrating fluids by serpentinites (Mubarak et al., 2020). The presence of granitic intrusions in the study area favors a hydrothermal source of the fluids that led to enrichment of some elements. The relatively high U and Sr can be attributed to the presence of Ca-bearing carbonates, while the enrichment in Pb is due to the presence of galena.

Chondrite-normalized patterns of REE concentrations in the serpentinite samples (Fig. 8b) show highly depleted and nearly parallel patterns. The total REE contents range between 0.97 and 1.12 μg/g in serpentinized harzburgite and 0.65 and 0.84 μg/g in serpentinized dunite (ST6). There is a gentle negative slope towards greater depletion in the less incompatible heavy rare earth elements compared to the more incompatible light rare earth elements. There are slight negative Eu anomalies in serpentinized harzburgite and slight positive Eu anomalies in serpentinized dunite.

6.2. Listvenites

Thirty-three representative listvenite samples (13 carbonate listvenite and 20 silica-carbonate listvenite) were analyzed for major oxides, trace elements, and rare-earth elements (Supplementary Table ST7). The different types of Tays listvenites show significant variability in their major oxides, in particular SiO_2, MgO, CaO, $Fe_2O_3^T$, K_2O and volatile contents (LOI) (Supplementary Table ST7). The SiO_2-(MgO + CaO)-Fe_2O_3 triangle variation diagram (Akbulut et al., 2006; Fig. 9a) clearly divides the samples into carbonate listvenite and silica-carbonate listvenite varieties.

Loss on ignition (LOI), which reflects the presence of H_2O or CO_2 in the samples, reaches its highest value in the carbonate listvenite (27.7–33.1 wt%) and is comparatively lower in the silica-carbonate listvenite (16.3–24.3 wt%), though still higher than in the serpentinite host (12.2–13.6 wt%). SiO_2 contents are 21.3–30.6 wt% in carbonate listvenite and 39.3–54.1 wt% in silica-carbonate listvenite (Fig. 9). MgO content decreases with increasing silica from carbonate listvenite (25.6–31.4 wt%) to silica-carbonate listvenite (16.0–23.0 wt%). CaO also decreases from carbonate listvenite (8.6–10.1 wt%) to silica-carbonate listvenite (6.2–7.7 wt%). The whole-rock CaO and MgO contents of carbonate listvenite samples are consistent with the dominance of magnesite over dolomite and calcite in these rocks. Total Fe_2O_3, like MgO and CaO, decreases from carbonate listvenite (4.5 to 6.0 wt%) to silica-carbonate listvenite (2.1–4.1 wt%). K_2O and Al_2O_3 increase with increasing silica from carbonate listvenite to silica-carbonate listvenite, and the samples of silica-carbonate listvenite containing visible fuchsite under the microscope have the highest contents of K_2O and Al_2O_3. Other oxides (TiO_2, Na_2O, and MnO) are low in all samples and do not correlate with lithology or other major oxides.

The concentrations of trace elements in the listvenite samples typically vary over about one order of magnitude (ST7). Both the carbonate-rich listvenite and the quartz-carbonate listvenite inherit from their protoliths considerable enrichment in Ni (1379–1778 μg/g and 1047–1454 μg/g), Cr (1364–1564 μg/g and 1313–2187 μg/g), Co (74–89 μg/g and 54–76 μg/g) and V (23–32 μg/g and 25–39 μg/g). The fluid-mobile elements (e.g., Au, Pb, Zn, Cu, Ag and As) are variably enriched, with in all cases much higher concentrations in silica-carbonate listvenite compared to carbonate listvenite (Fig. 10). Enrichment in Au is correlated with enrichment in the fluid-mobile elements. The primitive mantle-normalized trace element patterns of the listvenite samples (Fig. 11a) resemble in several aspects those of their serpentinite protoliths (Fig. 8a), but all the trace element contents are higher, by roughly a factor of four, and the peaks in Cs, Ba, U, and especially Pb and Sr are more pronounced. Most immobile trace element concentrations are lower in the silica-carbonate listvenite than in the carbonate listvenite, in marked contrast to the fluid-mobile elements. The distinctive enrichment in Pb in silica-carbonate listvenite is consistent with the observed presence of galena.

REE concentrations (ST7) and chondrite-normalized REE patterns (Fig. 11b) reveal that silica-carbonate listvenite has lower total REE contents (1.27–1.98 μg/g) than carbonate listvenite 2.05–2.88 μg/g). Both groups of listvenites have concave-up patterns, with middle REE depleted compared to both light and heavy REE; the pattern is more pronounced in the silica-carbonate listvenite. Carbonate listvenite samples show slight positive Eu anomalies (Eu/Eu* = 1.08–1.62), whereas silica-carbonate listvenite show slight negative Eu anomalies (0.71–0.95).

7. Discussion

7.1. Alteration and metamorphism

Metamorphism and subsequent alteration of the Tays ophiolites resulted in serpentinization, carbonation and listvenitization of these mantle rocks. Serpentinization of the peridotites was pervasive,

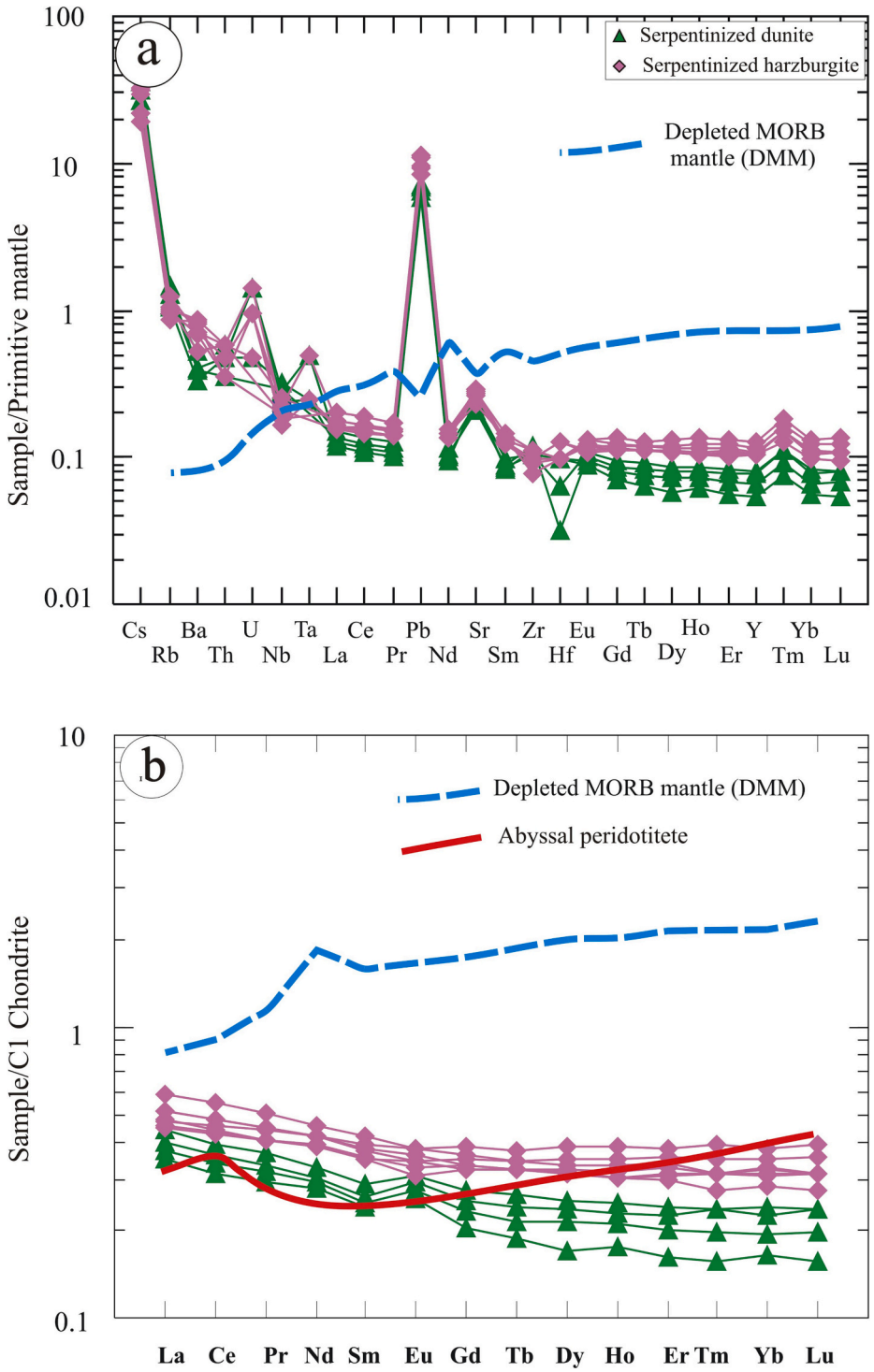

Fig. 8. Trace element contents of serpentinized peridotite. (a) Primitive mantle-normalized trace element patterns; normalization values from McDonough and Sun (1995). (b) Chondrite-normalized rare earth element patterns; normalization values from Evensen et al. (1978). The pattern of depleted MORB mantle (DMM) is adopted from Workman and Hart (2005), while the pattern of abyssal peridotite is adopted from Niu (2004).

affecting all the exposed ultramafic rocks and proceeding nearly to completion throughout the sequence. The other alteration processes are more localized, with formation of listvenite, talc-carbonate rocks, and magnesite confined along shear and fault planes. Similar patterns have been noted in a number of ophiolite occurrences in the ANS (e.g. Azer, 2014; Boskabadi et al., 2017; Abuamarah et al., 2020; Ali et al., 2023), but the timing of these alteration events and the sources of metasomatic fluids at each stage are still controversial. Gahlan et al. (2018) distinguished two episodes of listvenitization in the Gabal Sirsir ophiolite of the ANS: the first stage of listvenitization was contemporaneous with serpentinization of the oceanic lithosphere at a fore-arc spreading center, and the second stage occurred during emplacement of the ophiolite. Furthermore, Azer et al. (2019) distinguished two stages of carbonation in other ophiolites in the ANS: the first stage forms magnesite masses during deep-seated serpentinization (i.e. seafloor metamorphism) and subsequent metasomatism, whereas the second

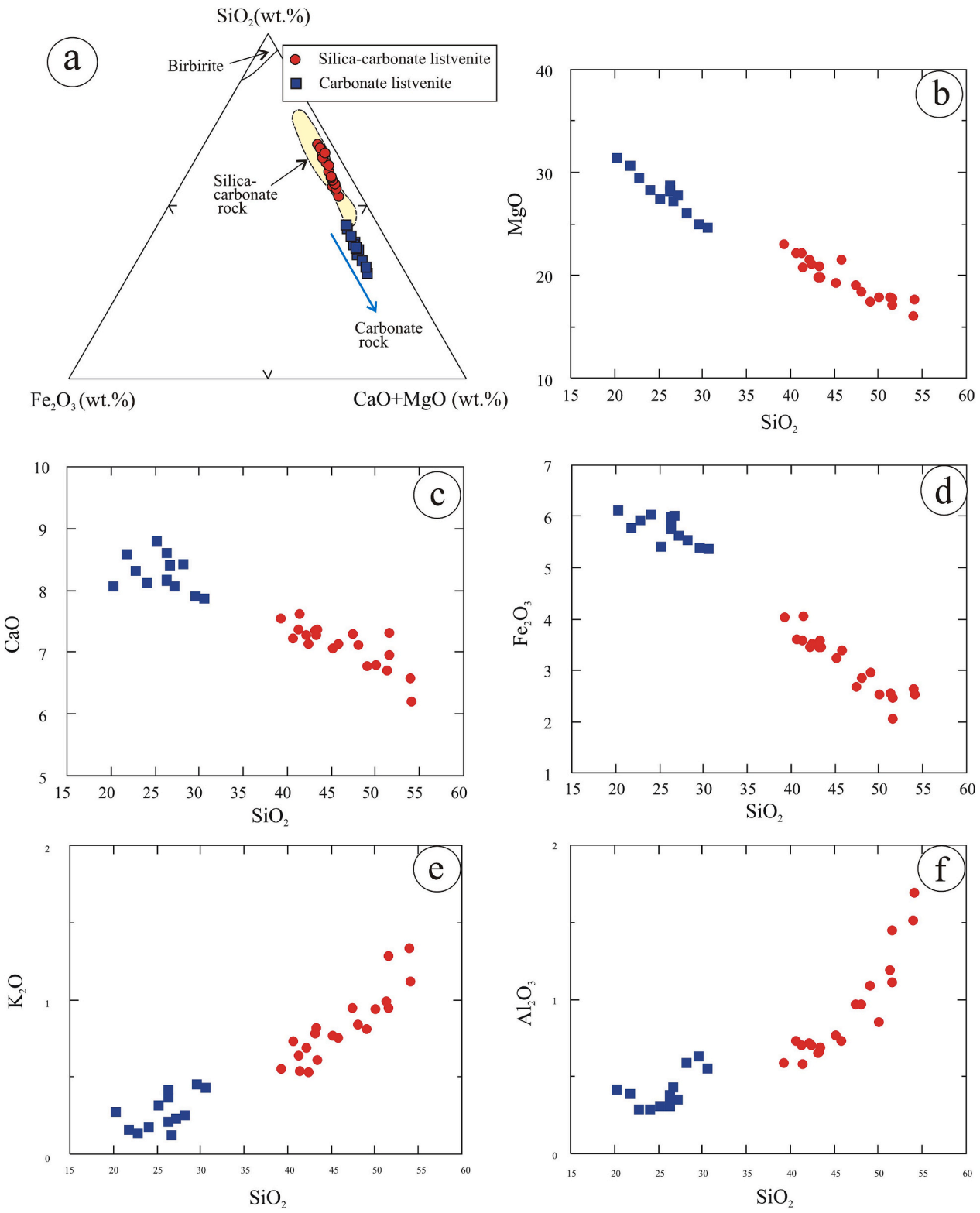

Fig. 9. Whole-rock major-element compositions of listvenites. (a) SiO_2-Fe_2O_3-(MgO+CaO) ternary diagram, (b–f) Harker SiO_2 variation diagrams.

stage witnesses the formation of carbonate veins after serpentinization and during the emplacement of the ophiolite.

7.2. Protolith and geodynamic setting of Tays serpentinites

Several petrogenetic models have been proposed for the geodynamic setting for ophiolitic rocks in the Arabian Shield; since their initial description, they have been attributed by one author or another to every setting where ocean crust might be produced, from open-ocean mid-ocean ridge to supra-subduction zone (e.g. Dilek and Ahmed, 2003; Ahmed et al., 2012; Habtoor et al., 2017). A general consensus has been reached that all the Arabian Shield ophiolites were formed above subduction zones (e.g. Johnson and Kattan, 2012; Shahien et al., 2021). However, discussion has continued around attempts to distinguish

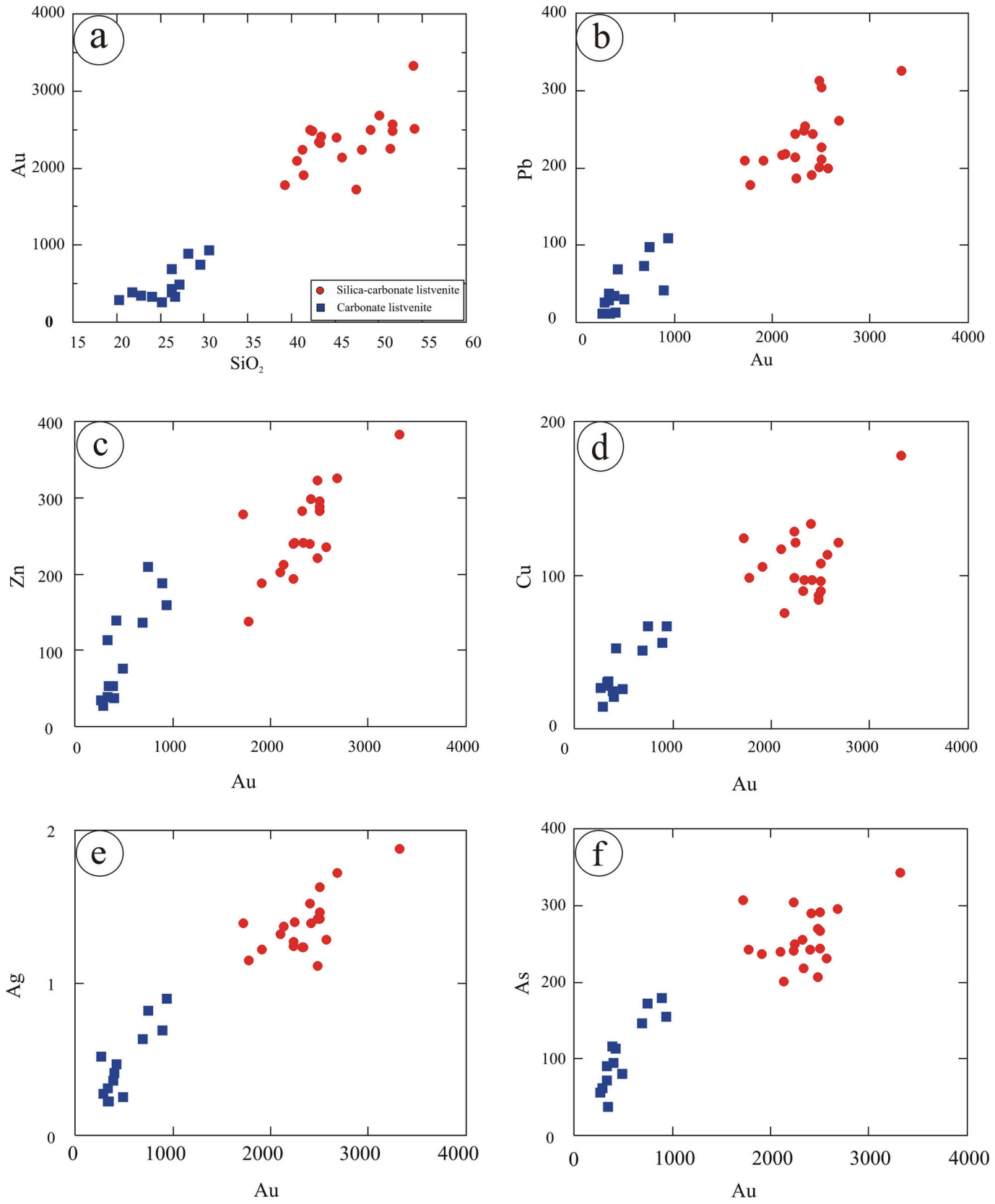

Fig. 10. Bivariate diagrams of elemental concentration in listvenite samples showing correlations of Au enrichment with SiO_2 and fluid-mobile elements Pb, Zn, Cu, Ag, and As.

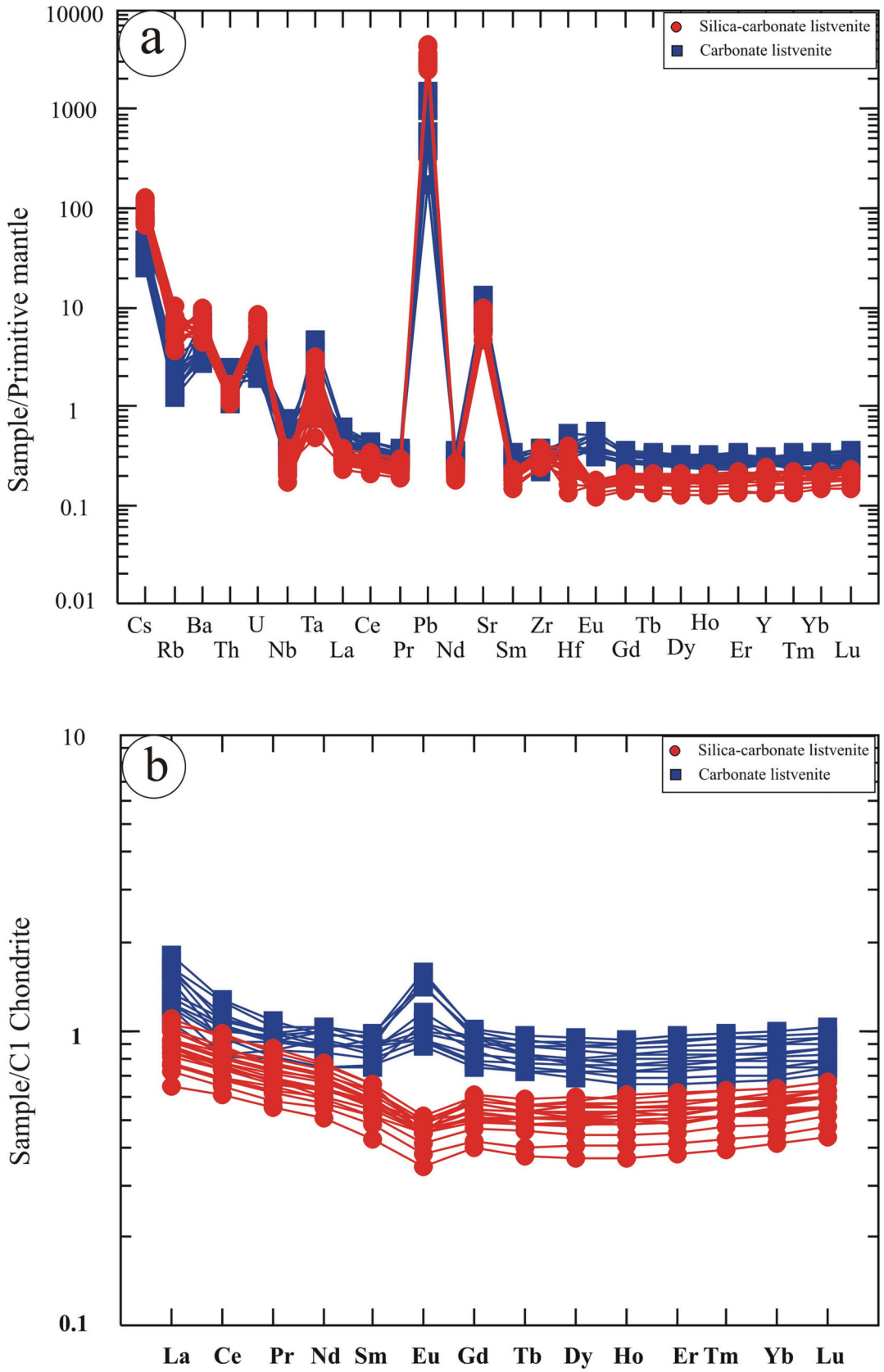

Fig. 11. Trace element contents of listvenites. (a) Primitive mantle-normalized trace elements (McDonough and Sun, 1995). (b) Chondrite-normalized rare earth element patterns (Evensen et al., 1978).

whether they formed in back-arc or fore-arc settings. Recently, based on mineral compositions of fresh relics of primary silicate minerals (olivine and pyroxenes) and Cr-spinel, it has been repeatedly shown that the mantle sections of the Arabian Shield ophiolites represent residues after extensive degrees of partial melting that most closely resemble peridotites dredged or drilled from fore-arc settings (Abuamarah et al., 2020, 2023; Gahlan et al., 2021).

The Tays serpentinites are typical of the mantle sections of the Arabian Shield ophiolites. Petrographic examination reveals mesh and bastite textures (Fig. 3d, e) after olivine and orthopyroxene in proportions indicating mostly harzburgite and some dunite protoliths. Their normative mineralogy based on whole-rock chemistry confirms this inference (Fig. 7a). Moreover, their high compatible element (Cr, Ni, Co) concentrations, high Mg# (0.91–0.92), and low concentrations of incompatible oxides (TiO_2, Al_2O_3, CaO) and fluid-immobile trace elements all resemble the characteristics of refractory mantle residues after high degrees of partial melt extraction (Deschamps et al., 2013; Salters and Stracke, 2004). On the MgO/SiO_2 vs. Al_2O_3/SiO_2 diagram (Fig. 7b), the serpentinized harzburgite samples plot at low Al_2O_3/SiO_2 in the area of overlap between fore-arc peridotite and depleted abyssal peridotites (e.g., Deschamps et al., 2013), whereas the dunites may have had their MgO/SiO_2 ratio increased by melt-rock reaction processes that are not well-represented in sea-floor peridotite suites (e.g., Kelemen, 1990). In Al_2O_3 vs. CaO space, all the Tays serpentinite samples plot in the fore-arc field (Fig. 7c). The most recent overall model for the evolution of the ANS ophiolites in a fore-arc setting was proposed by Abdel-Karim et al. (2021a). This model can be adopted for the evolution of the Tays ophiolite. It shows the several stages required to generate the Arabian Shield ophiolites (Fig. 12).

Serpentinization is thought to occur early in the evolution of fore-arc residual mantle lithosphere, due to the continuing flux of slab-derived fluid. The alteration of Cr-spinel to form ferritchromite and Cr-magnetite rims and the present of disseminated magnetite indicate that oxidation of Fe^{2+} accompanied serpentinization, likely coupled to reduction of H_2O to H_2 (Klein et al., 2017; Mével, 2003).

7.3. Petrogenesis of Tays listvenites

The two varieties of listvenite found in the Tays ophiolite record a multistage history of transformation of the primary ultramafic rocks through serpentinization, carbonation and silicification. Each of these alteration processes requires the action of a fluid phase to introduce some chemical components and remove others. The absence of felsic intrusions associated with the listvenites and their distribution along thrust planes argue against magmatic fluid sources. The process of listvenitization has been attributed by various authors to several potential

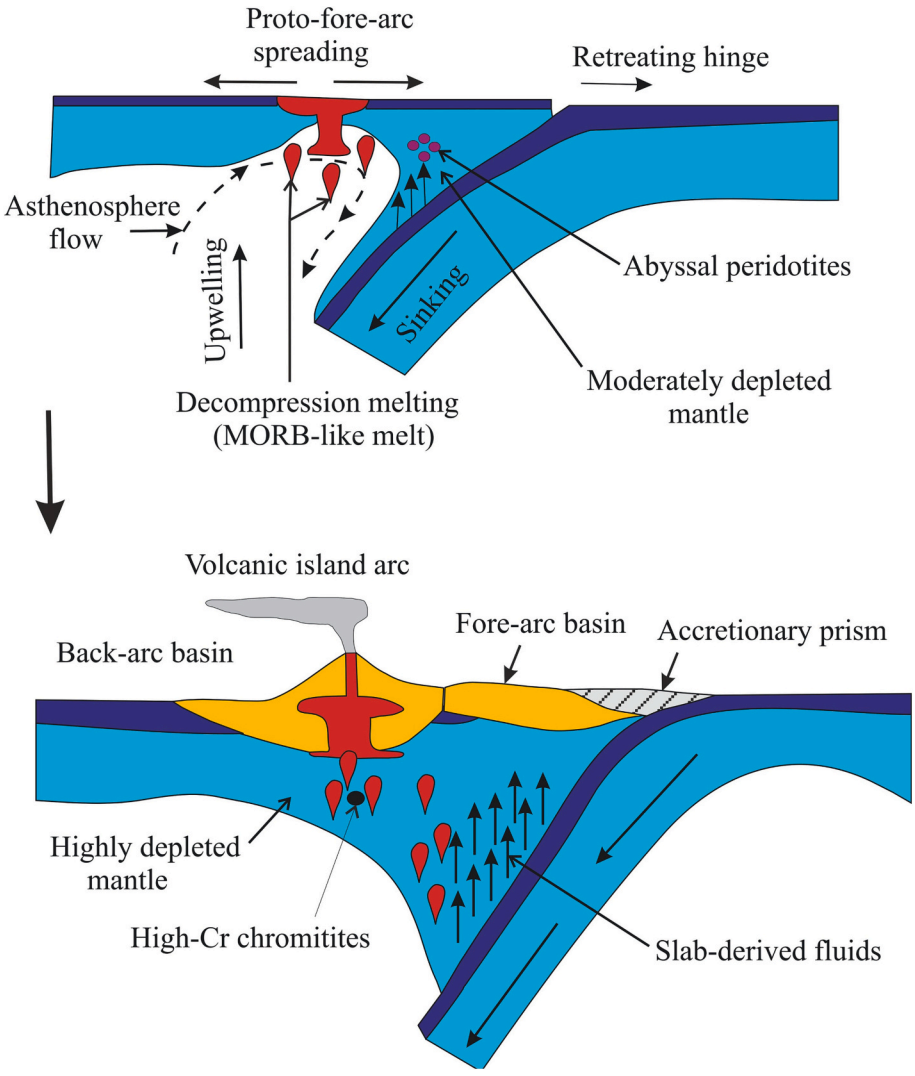

Fig. 12. Schematic illustration showing the stages in generation of ophiolites of the Arabian Shield, from subduction initiation with fore-arc spreading to mature subduction (after Abdel-Karim et al., 2021a). Not shown: subsequent reversal of thrust vergence and obduction of the fore-arc ophiolite over the island-arc sequence.

metasomatic agents: (1) mantle-derived CO_2-bearing fluids infiltrating the oceanic lithosphere (e.g., Stern and Gwinn, 1990; Boskabadi et al., 2017; Hamdy and Gamal El Dien, 2017), (2) meteoric and metamorphic hydrothermal fluids penetrating along tectonic fractures during exhumation to upper crustal levels (e.g., Buisson and Leblanc, 1987; Hamdy and Lebda, 2007), and (3) mixing of these two sources (e.g., Gahlan et al., 2018).

Field and microscopic evidence shows that the two varieties of listvenite represent two successive stages of alteration of the ultramafic precursors. The carbonate minerals in the carbonate listvenite display considerable microscopic evidence of deformation, such as kink banding, fragmentation, and recrystallization into fine-grained aggregates. The macroscopic schistosity of the carbonate listvenite and the microscopic shear indicators are both structurally concordant with fabrics in their serpentinite hosts. However, the carbonate listvenite is also distributed along shear planes. Together, the structural evidence indicates that initial listvenitization accompanied shear deformation of the serpentinite hosts. Most probably this occurred during seafloor metamorphism (i.e., serpentinization). The alteration of primary Cr-spinel to ferritchromite is noted in both serpentinite and carbonate listvenite and indicates that serpentinization (and associated hydrogen production and Fe oxidation) affected the protolith of the carbonate listvenite. The carbonate listvenite records the action of CO_2-bearing fluids released during serpentinization of the original peridotite in a fore-arc setting (as indicated by the geochemistry of host serpentinite). By contrast, the absence of macroscopic schistosity and the petrographic evidence of a second generation of undeformed quartz and carbonate minerals in the silica-carbonate listvenite suggest that its formation post-dates serpentinization and represents a distinct and later second phase of alteration. The presence of a first generation of deformed quartz and carbonate minerals in silica-carbonate listvenite indicates that it formed by further transformation from carbonate listvenite that developed in the first stage. We infer that the second stage of listvenitization accompanied the obduction of the Tays ophiolite along the thrust planes. At this phase, the source of SiO_2-saturated metasomatic fluids is likely the continental shelf or magmatic arc sequences in the footwall of the obduction thrust.

Compared to the samples of serpentinite that probably indicate the protolith composition, all the listvenite varieties are enriched in CaO, K_2O and Na_2O, but depleted in MgO. Listvenite samples display relative enrichment in Sr, Ba, Rb, Zn, Pb, As, U, Ta, Au, Ag, Cs and Sb. The most notable gains are in Au, Pb, Zn, Sb and As. Some other elements appear to be immobile and remain nearly equal in listvenite and serpentinite (Cr, Co, V, Ni, Sc and Ga). The correlation between enrichment in fluid-mobile elements and silica content implies that more extensive reaction with silicifying fluid yields the most silica-rich and fluid-modified samples. The extreme end-product of this process is likely preserved by the (unsampled) thin cap of silica-rich listvenite observed in some places. Mineralogically, the presence of fuchsite in the silica-carbonate listvenite indicates enrichment in K in this metasomatic fluid (Peng et al., 2020; Pirouei et al., 2020; Moussa et al., 2021). The remarkable Sr enrichment in a limited number of silica-carbonate listvenite samples may also reflect a Sr-rich character in this fluid. Also, enrichment of Sr is well documented as a process that occurs during serpentinization (Deschamps et al., 2010).

We find that listvenitization concentrates gold in the alteration products to grades that may well reach economic proportions. Sulfides are abundant in the listvenite, especially the gold-bearing samples. This suggests that mobilization of gold in the fluid is associated with complexation by sulfur and that crystallization of solid sulfides provides a host to immobilize and concentrate Au and associated metals (Gahlan et al., 2020a). It is also notable that (unlike both serpentinite and carbonate listvenite), silica-carbonate listvenite samples lack ferritchromite rims on their Cr-spinel relics. This suggests that ferritchromite was resorbed during the final alteration stage, possibly due to reduction of the previously oxidized Fe.

The most notable Au enrichment is found specifically in silica-carbonate listvenite. Given that different fluid sources, with different pH and fO_2, were involved in the two stages of listvenitization, it would be something of a coincidence if both processes independently concentrated Au. Instead, the most probable pathway to the strong enrichment of Au in silica-carbonate listvenite is remobilization of the Au pre-concentrated in carbonate listvenite. Hence, consistent with the presence of two generations (deformed and un-deformed) of quartz and carbonate minerals, we conclude that silica-carbonate listvenite developed by further alteration of carbonate listvenite rather than forming from previously un-enriched serpentinite. This requires reactivation at the ophiolite emplacement stage of the fluid pathways along the shear planes previously developed during serpentinization, as preferred conduits for the late mineralizing fluid.

8. Conclusions

- The mantle section of the Late Neoproterozoic Tays ophiolite (Arabian Shield) contains variably serpentinized peridotites that are highly altered along shear zones and thrust planes to form gold-bearing listvenite bodies of various shapes and sizes. The bulk and mineral compositions of the Tays serpentinized peridotite indicate a depleted mantle protolith associated with fore-arc setting.
- The listvenite bodies are petrographically and geochemically distinguished into two major varieties; namely carbonate listvenite and silica-carbonate listvenite. Carbonate listvenite is composed mainly of carbonate minerals (60–85 %) and quartz (15–40 %) with Fe-Ti oxides, Cr-spinel partly altered to ferritchromite, and sulfides. Silica-carbonate listvenite consists mainly of quartz (55–65 %) and carbonate (35–45 %) with minor amounts of serpentine, chlorite, Cr-rich muscovite (fuchsite), sulfides, goethite and Cr-spinel (without ferritchromite).
- Carbonate listvenite is characterized by the presence of schistosity and deformation fabrics similar to the host serpentinite that suggests its formation predates deformation of the whole sequence. It is attributed to infiltration of CO_2-bearing fluids released during serpentinization of the original fore-arc peridotite.
- The absence of deformation fabrics in silica-carbonate listvenite suggests that its formation postdates serpentinization, carbonate listvenite and associated deformation. It is attributed to the activity of K-bearing, SiO_2-saturated fluids released during the obduction of the ophiolite.
- Silica-carbonate listvenite is characterized by the presence of fuchsite, sulfides, and specks of gold. Chemically, it is enriched in fluid-mobile elements Zn, Pb, Cu, Ag, and most notably Au; this enrichment is correlated with silica content. Listvenitization concentrated gold in sub-economic to economic proportions, especially in silica-carbonate listvenite (1717–3324 ng/g), compared to the low-grade Au concentration in the carbonate listvenite (267–937 ng/g) and the serpentinite protolith (1.95–4.14 ng/g).

Supplementary data to this article can be found online at https://doi.org/10.1016/j.chemer.2024.126081.

CRediT authorship contribution statement

Fahad Alshehri: Supervision, Resources, Project administration, Funding acquisition. **Mokhles K. Azer:** Writing – review & editing, Visualization, Validation, Supervision, Software, Conceptualization. **Paul D. Asimow:** Writing – review & editing, Validation, Investigation, Formal analysis, Conceptualization. **Bassam A. Abuamarah:** Writing – review & editing, Validation, Software, Resources, Data curation.

Declaration of competing interest

The authors declare that they have no known competing financial

interests or personal relationships that could have appeared to influence the work reported in this paper.

Acknowledgements

The authors extend their appreciation to the Deputyship for Research & Innovation, Ministry of Education in Saudi Arabia, for funding this research work through project no. IFKSURC-1-7310.

References

Abdel-Karim, A., El-Shafei, S., Azer, M., 2021a. The Neoproterozoic ophiolitic ultramafic rocks in Eastern Desert of Egypt: implications for petrogenesis and metasomatic processes. International Geology Review 63 (2), 208–232.

Abdel-Karim, A.M., El-Shafei, S.A., Azer, M.K., 2021b. Petrology and geochemistry of ophiolitic metaperidotites from the Eastern Desert of Egypt: insights into geodynamic evolution and post-melting alteration processes. Acta Geol. Sin. 95 (4), 1139–1157.

Abuamarah, B.A., Asimow, P.D., Azer, M.K., Ghrefat, H., 2020. Suprasubduction-zone origin of the podiform chromitites of the Bir Tuluhah ophiolite, Saudi Arabia, during Neoproterozoic assembly of the Arabian shield. Lithos 360–361, 105439.

Abuamarah, B.A., Alshehri, F., Azer, M.K., Asimow, P.D., 2023. Geological and Tectonic Significance of Rodingite in the Ess Ophiolite. Lithos, Arabian Shield, Saudi Arabia, p. 107168.

Ahmed, A.H., Harbi, H.M., Habtoor, A.M., 2012. Compositional variations and tectonic settings of podiform chromitites and associated ultramafic rocks of the Neoproterozoic ophiolite at Wadi Al Hwanet, northwestern Saudi Arabia. J. Asian Earth Sci. 56, 118–134.

Akbulut, M., Pişkin, Ö., Karayiğit, A.İ., 2006. The genesis of the carbonatized and silicified ultramafics known as listvenites: a case study from the Mihalıççık region (Eskişehir). NW Turkey. Geological Journal 41 (5), 557–580.

Al Jahdali, N.S., 2004. Geology of Jabal Ghadarah Area, Bir Tawilah District with Special Emphasis on Listvenite as a Potential Source for Gold in the Kingdom of Saudi Arabia. Thesis, King AbdulAziz University, Jeddah, KSA, M.Sc (197p).

Al Jahdali, N.S., Harbi, H., Eldougdoug, A., 2003. Gold bearing listvenite in Jabal Al Ghadarah area, central Arabian Sheild, Kingdom of Saudi Arabia. In: Proceedings of the 8th Arab Conference on Mineral Resources, Sanaá. Republic of Yemen, 13-16 October, 1, pp. 26–43.

Al Shanti, A.M.S., 2009. Geology of the Arabian Shield of Saudi Arabia. Scientific Publications Centre, King Abdulaziz University, Jeddah, KSA.

Ali, K.A., Azer, M.K., Gahlan, H.A., Wilde, S.A., Samuel, M.D., Stern, R.J., 2010. Age of formation and emplacement of Neoproterozoic ophiolites and related rocks along the Allaqi suture, south Eastern Desert. Egypt. Gondwana Research 18, 583–595.

Ali, R.A., Pitcairn, I.K., Maurice, A.E., Azer, M.K., Bakhit, B.R., Shahien, M.G., 2020. Petrology and geochemistry of ophiolitic ultramafic rocks and chromitites across the Eastern Desert of Egypt: insights into the composition and nature of a Neoproterozoic mantle and implication for the evolution of SSZ system. Precambrian Res. 337, 105565.

Ali, S., Azer, M., Abdel-Karim, A.A., 2023. Origin and evolution of Neoproterozoic metaophiolitic mantle rocks from the eastern desert of Egypt: implications for tectonic and metamorphic events in the Arabian-Nubian shield. Geol. Acta 21 (6), 1–21 (I-VII).

Azer, M.K., 2013. Evolution and economic significance of listwaenites associated with Neoproterozoic ophiolites in south Eastern Desert. Egypt. Geologica Acta 11 (1), 113–128.

Azer, M.K., 2014. Petrological studies of Neoproterozoic serpentinized ultramafics of the Nubian shield: spinel compositions as evidence of the tectonic evolution of the Egyptian ophiolites. Acta Geol. Pol. 64, 113–127.

Azer, M.K., Stern, R.J., 2007. Neoproterozoic (835-720 Ma) serpentinites in the Eastern Desert, Egypt: fragments of fore-arc mantle. J. Geol. 115, 457–472.

Azer, M.K., Samuel, M.D., Ali, K.A., Gahlan, H.A., Stern, R.J., Ren, M., Moussa, H.E., 2013. Neoproterozoic ophiolitic peridotites along the Allaqi–Heiani Suture, South Eastern Desert, Egypt. Mineralogy and Petrology 107 (5), 829–848.

Azer, M.K., Gahlan, H.A., Asimow, P.D., Mubarak, H.S., Al-Kahtany, K.M., 2019. Multiple stages of carbonation and element redistribution during formation of ultramafic-hosted magnesite in Neoproterozoic ophiolites of the Arabian-Nubian shield. Egypt. The Journal of Geology 127 (1), 81–107.

Bonatti, E., Michael, P.J., 1989. Mantle peridotites from continental rifts to oceanic basins to subduction zones. Earth Planet. Sci. Lett. 91, 297–311.

Boskabadi, A., Pitcairn, I.K., Broman, C., Boyce, A., Teagle, D.A.H., Cooper, M.J., Azer, M.K., Mohamed, F.H., Stern, R.J., Majka, J., 2017. Carbonate alteration of ophiolitic rocks in the Arabian–Nubian Shield of Egypt: sources and compositions of the carbonating fluid and implications for the formation of Au deposits. International Geology Review 59 (4), 391–419.

Boyle, R.W., 1979. The geochemistry of gold and its deposits. Geological Survey of Canada Bulletin 280, 333–361.

Buisson, G., Leblanc, M., 1986. Gold-bearing listwaenites (carbonatized ultramafic rocks) from ophiolite complexes. In: Gallagher, J.M., Ixer, R.A., Neary, C.R. (Eds.), Metallogeny of Basic and Ultrabasic Rocks. Institution of Mining and Metallurgy, London, pp. 121–132.

Buisson, G., Leblanc, M., 1987. Gold in mantle peridotites from upper Proterozoic ophiolites in Arabia, Mali, and Morocco. Econ. Geol. 82 (8), 2091–2097.

Cox, G.M., Lewis, C.J., Collins, A.S., Halverson, G.P., Jourdan, F., Foden, J., Nettle, D., Kattan, F., 2012. Ediacaran terrane accretion within the Arabian–Nubian Shield. Gondw. Res. 21 (2–3), 341–352.

Deschamps, F., Guillot, S., Godard, M., Chauvel, C., Andreani, M., Hattori, K., 2010. In situ characterization of serpentinites from forearc mantle wedges: timing of serpentinization and behavior of fluid-mobile elements in subduction zones. Chem. Geol. 269 (3–4), 262–277.

Deer, W.A., Howie, R.A., Zussman, J., 1992. An introduction to the rock forming minerals, Second Edition. Longman Scientific and Technical, London, p. 696.

Deschamps, F., Godard, M., Guillot, S., Hattori, K., 2013. Geochemistry of subduction zone serpentinites: a review. Lithos 178, 96–127.

Dilek, Y., Ahmed, Z., 2003. Proterozoic ophiolites of the Arabian shield and their significance in Precambrian tectonics. In: Dilek, Y., Robinson, P.T. (Eds.), Ophiolites in Earth History, Geological Society of London Special Pub, vol. 218, pp. 685–700.

Evensen, N.M., Hamilton, P.J., O'Nions, R.K., 1978. Rare earth abundances in chondritic meteorites. Geochim. Cosmochim. Acta 42 (8), 1199–1212.

Gahlan, H.A., Azer, M.K., Khalil, A.E., 2015. The Neoproterozoic Abu Dahr ophiolite, south Eastern Desert, Egypt: petrological characteristics and tectonomagmatic evolution. Mineral. Petrol. 109, 611–630.

Gahlan, H.A., Azer, M.K., Asimow, P.D., 2018. On the relative timing of listwaenite formation and chromian spinel equilibration in serpentinites. Am. Mineral. 103 (7), 1087–1102.

Gahlan, H.A., Azer, M.K., Asimow, P.D., Al-Kahtany, K.M., 2020a. Petrogenesis of gold-bearing listvenites from the carbonatized mantle section of the Neoproterozoic Ess ophiolite, Western Arabian shield. Saudi Arabia. Lithos 372, 105679.

Gahlan, H.A., Azer, M.K., Asimow, P.D., Mubarak, H.S., Al-Kahtany, K.M., 2020b. Petrological characteristics of the Neoproterozoic Ess ophiolite mantle section, Arabian shield, Saudi Arabia: a mineral chemistry perspective. Int. J. Earth Sci. 109, 239–251.

Gahlan, H.A., Azer, M.K., Asimow, P.D., Al-Kahtany, K.M., 2020c. Genesis and geodynamic evolution of serpentinized ultramafics and associated magnesite deposits in the Al-Wask ophiolite, Arabian shield, Saudi Arabia. Am. J. Sci. 320, 236–279.

Gahlan, H.A., Azer, M.K., Al-Kahtany, K.M., 2021. Petrogenesis and geodynamic setting of high-Cr chromitites in fore-arc peridotites: A case study from the Halaban ophiolite, eastern Arabian shield. Saudi Arabia. Lithos 396–397, 106243.

Gahlan, H.A., Azer, M.K., Asimow, P.D., Al-Kahtany, K.M., 2022. Formation of gold-bearing listvenite in the mantle section of the Neoproterozoic Bir Umq ophiolite, Western Arabian shield, Saudi Arabia. J. Afr. Earth Sci. 190, 104517.

Habtoor, A.M., Ahmed, A.H., Akizawa, N., Harbi, H., Arai, S., 2017. Chemical homogeneity of high-Cr chromitites as indicator for widespread invasion of boninitic melt in mantle peridotite of Bir Tuluha ophiolite. Northern Arabian Shield, Saudi Arabia Ore Geology Reviews 90, 243–259.

Halls, C., Zhao, R., 1995. Listvenite and related rocks: perspectives on terminology and mineralogy with reference to an occurrence at Cregganbaun, Co. Mayo, Republic of Ireland. Miner. Deposita 30 (3–4), 303–313.

Hamdy, M.M., Gamal El Dien, H.M., 2017. Nature of serpentinization and carbonation of ophiolitic peridotites (Eastern Desert, Egypt): constrains from stable isotopes and whole rock geochemistry. Arabian Journal of Geoscience 10 (19), 429.

Hamdy, M.M., Lebda, E.M., 2007. Metamorphism of ultramafic rocks at Gebel Arais and Gebel Malo grim, Eastern Desert, Egypt: mineralogical and O-H stable isotopic constraints. Egypt. J. Geol. 51, 105–124.

Harbi, H., Eldougdoug, A., Al Jahdali, N.S., 2006. Geology and geochemistry of Jabal Ghadarah Ophiolitic mélange, Zalim quadrangle, Central Saudi Arabia. Journal of King Abdulaziz University (Earth Sciences) 17, 117–153.

Hart, S.R., Zindler, A., 1986. In search of a bulk-earth composition. Chem. Geol. 57, 247–267.

Ishii, T., Robinson, P.T., Maekawa, H., Fiske, R., 1992. Petrological studies of peridotites from diapiric Serpentinite Seamounts in the Izu-Ogasawara-Mariana forearc, leg 125. In: Pearce, J., Stokking, L.B., et al. (Eds.), Proceedings of the Ocean Drilling Project, Leg 125, Scientific Results (College Station), pp. 445–485.

Jagoutz, E., Palme, H., Baddenhausen, H., Blum, K., Cendales, M., Dreibus, G., Spettel, B., Lorenz, V., Vanke, H., 1979. The abundance of major, minor and trace elements in the earth's mantle as derived from primitive ultramafic nodules. Geochim. Cosmochim. Acta 11, 2031–2050.

Johnson, P.R., Kattan, F.H., 2012. The geology of the Saudi Arabian shield. Saudi Geological Survey, 512 Internal Report.

Johnson, P.R., Stewart, I.C., 1995. Magnetically inferred basement structure in Central Saudi Arabia. Tectonophysics 245 (1–2), 37–52.

Johnson, P.R., Kattan, F.H., Al-Saleh, A.M., 2004. Neoproterozoic ophiolites in the Arabian shield: field relations and structure. Developments in Precambrian Geology 13, 129–162.

Kelemen, P.B., 1990. Reaction between ultramafic rock and fractionating basaltic magma I. Phase relations, the origin of Calc-alkaline magma series, and the formation of discordant dunite. J. Petrol. 31, 51–98.

Kennedy, A., Kozdroj, W., Johnson, P.R., Kattan, F.H., 2011. SHRIMP Geochronology in the Northern Arabian Shield. Part III: Data acquisition, 2006. Saudi Geological Survey Open-File Report SGS-OF-2007-9.

Khalil, A.E.S., Obeid, M.A., Azer, M.K., 2014. Serpentinized peridotites at the north part of Wadi Allaqi district (Egypt): implications for the tectono-magmatic evolution of fore-arc crust. Acta Geol. Sin. 88 (5), 1421–1436.

Klein, F., Marschall, H.R., Bowring, S.A., Humphris, S.E., Horning, G., 2017. Mid-ocean ridge serpentinite in the Puerto Rico Trench: From seafloor spreading to subduction. J. Petrol. 58 (9), 1729–1754.

McDonough, W.F., Sun, S.S., 1995. Composition of the Earth: Chemical Geology 120, 223–253.

Mével, C., 2003. Serpentinization of abyssal peridotites at mid-ocean ridges. C. R. Geosci. 335 (10–11), 825–852.
Moussa, H.E., Azer, M.K., Abou El Maaty, M.A., Maurice, A.E., Yanni, N.N., Akarish, A.I., Elnazer, A.A., Elsagheer, M.A., 2021. Carbonation of Neoproterozoic mantle section and formation of gold-bearing listvenite in the northern Nubian shield. Lithos 406, 106525.
Moussa, H.E., Mubarak, H.S., Azer, M.K., Surour, A.A., Asimow, P.D., Kabesh, M.M., 2022. Multistage petrogenetic evolution of Neoproterozoic serpentinized ultramafic rocks and podiform chromitites at Hagar Dungash. Eastern Desert of Egypt. Precambrian Research 369, 106507.
Mubarak, H.S., Azer, M.K., Surour, A.A., Moussa, H.E., Asimow, P.D., Kabesh, M.M., 2020. Mineralogical and geochemical study of rodingites and associated serpentinized peridotite, Eastern Desert of Egypt. Arabian-Nubian Shield. Lithos 374, 105720.
Nehlig, P., Genna, A., Asfirane, F., 2002. A review of the Pan-African evolution of the Arabian shield. GeoArabia 7, 103–124.
Niu, Y., 2004. Bulk-rock major and trace element compositions of abyssal peridotites: implications for mantle melting, melt extraction and post-melting processes beneath mid-ocean ridges. J. Petrol. 45, 2423–2458.
Obeid, M.A., Khalil, A.E.S., Azer, M.K., 2016. Mineralogy, geochemistry and geotectonic significance of the Neoproterozoic ophiolite of Wadi Arais area, south Eastern Desert. Egypt. International Geology Reviews 58, 687–702.
Parkinson, I.J., Pearce, J.A., 1998. Peridotites from the Izu-Bonin-Mariana forearc (ODP leg 125): evidence for mantle melting and melt-mantle interaction in a supra-subduction zone setting. J. Petrol. 39, 1577–1618.
Pearce, J.A., Barker, P.F., Edwards, S.J., Parkinson, I.J., Leat, P.T., 2000. Geochemistry and tectonic significance of peridotites from the South Sandwich arc-basin system, South Atlantic. Contribution to Mineralogy and Petrology 139, 36–53.
Peng, W., Zhang, L., Menzel, M.D., Brovarone, A.V., Tumiati, S., Shen, T., Hu, H., 2020. Multistage CO2 sequestration in the subduction zone: insights from exhumed carbonated serpentinites, SW Tianshan UHP belt, China. Geochim. Cosmochim. Acta 270, 218–243.
Pirouei, M., Kolo, K., Kalaitzidis, S.P., 2020. Chromium-rich muscovite mineralization in Zagros ophiolites in Iraqi Kurdistan: a study on fuchsite paragenetic association with listvenite types. Arab. J. Geosci. 13, 1–13.
Plissart, G., Féménias, O., Măruntiu, M., Diot, H., Demaiffe, D., 2009. Mineralogy and geothermometry of gabbro-derived listvenites in the Tisovita–Iuti ophiolite, Southwestern Romania. Canadian Mineralogist 47 (1), 81–105.
Rose, G., 1837. Mineralogisch-geognostische reise nach dem Ural, dem Altai und dem Kaspischen Meere. In: Reise nach dem nordlichen Ural und dem Altai 1. Verlag der Sanderschen Buchhandlung, Berlin.
Salters, V.J., Stracke, A., 2004. Composition of the depleted mantle. Geochem. Geophys. Geosyst. 5 (5).
Sepidbar, F., Lucci, F., Biabangard, H., Zaki Khedr, M., Jiantang, P., 2020. Geochemistry and tectonic significance of the Fannuj-Maskutan SSZ-type ophiolite (Inner Makran, SE Iran). Int. Geol. Rev. 62 (16), 2077–2104.
Shahien, M.G., Azer, M.K., Asimow, P.D., 2021. Neoproterozoic ophiolites of the Arabian-Nubian Shield. In: Hamimi, Z., Fowler, A.-R., Liegeois, J.-P., Collins, A., Abdelsalam, M., Abd El-Wahed, M. (Eds.), The Geology of the Arabian-Nubian Shield. Springer (ISBN 978-3-030-72994-3).
Stern, R.J., Gwinn, C.J., 1990. Origin of late Precambrian intrusive carbonates, Eastern Desert of Egypt and Sudan: C, O and Sr isotopic evidence. Precambrian Res. 46 (3), 259–272.
Uçurum, A., 2000. Listwaenites in Turkey: perspectives on formation and precious metal concentration with reference to occurrences in east-central Anatolia. Ofioliti 25 (1), 15–29.
Workman, R.K., Hart, S.R., 2005. Major and trace element composition of the depleted MORB mantle (DMM). Earth Planet. Sci. Lett. 231 (1–2), 53–72.